Journal of Materials Chemistry A

ROYAL SOCIETY OF CHEMISTRY

PAPER

View Article Online
View Journal

Cite this: DOI: 10.1039/d5ta10103d

A multifunctional flexible SnTe/MWCNT crystalline hybrid for energy storage and humidity sensing with 3D-printed device integration

Mohammad Saquib,[a] Shilpa Shetty,[a] Manasa R. Shankar,[b] A. N. Prabhu,[b] Ramakrishna Nayak,[c] M. S. Santosh[d] and M. Selvakumar *[a]

The design of multifunctional materials that unify energy storage and environmental sensing is vital for next-generation flexible electronics and IoT devices. Here, the first report of a Bridgman-grown polycrystalline SnTe/MWCNT (SUM) hybrid is presented, where the high pseudocapacitance of SnTe is synergistically coupled with the conductivity, flexibility, and porous architecture of carbon nanotubes. This hybrid serves as a dual-function platform, enabling both high-performance microsupercapacitors and humidity sensors fabricated *via* scalable screen-printing. The optimized asymmetric device (FAM–SUM-10) delivers an areal capacitance of 468.6 mF cm^{-2}, >90.7% retention at high scan rates, and excellent cycling stability (95.3% coulombic efficiency over 10 000 cycles) under mechanical deformation. As a humidity sensor, the same SUM-10 composite exhibits fast response (7 s), short recovery (9 s), and high sensitivity and is further integrated into a 3D-printed wireless module for real-time monitoring. This work establishes Bridgman-assisted hybridization as a versatile route for scalable, flexible materials that bridge energy storage and environmental intelligence in wearable and precision sensing applications.

Received 10th December 2025
Accepted 8th March 2026

DOI: 10.1039/d5ta10103d

rsc.li/materials-a

1. Introduction

The rapid depletion of non-renewable energy resources, particularly fossil fuels, has accelerated the search for sustainable and eco-friendly alternatives. Excessive reliance on these resources has led to significant environmental degradation, global economic challenges, and energy insecurity.[1–4] Consequently, research efforts have increasingly focused on renewable energy technologies, including energy conversion and storage devices, to meet the demands of modern society. Flexible microsupercapacitors (FMSCs) have emerged as a cutting-edge solution in this field, offering compact, lightweight, and durable energy storage options suitable for integration into wearable electronics, portable devices, and flexible energy systems.[5–10] They exhibit various advantageous properties such as exceptional power density, rapid charge/discharge capability, and extended cycle life.[11,12] Conventional supercapacitors, including MSCs, are known for their exceptional power density, rapid charge–discharge capability, and extended cycle life, distinguishing them from conventional capacitors and batteries.[13,14] Although FMSCs offer notable benefits, a major hurdle lies in boosting their energy density without compromising their flexibility or other key characteristics. Beyond FMSCs, the rapid advancement of Internet of Things (IoT) and artificial intelligence (AI) technologies has driven the widespread deployment of smart sensors, fundamentally transforming environmental monitoring and human–machine interactions.[15,16] Humidity sensors (HSs), as a vital category of smart sensing devices, are widely employed in diverse areas, including human–machine interfaces,[17] healthcare monitoring,[18] and safety inspections in industrial environments.[19] Elevated humidity levels above 60% can promote the proliferation of harmful microorganisms, cause discomfort,[20] and result in the deterioration of buildings and electronic devices. Conversely, low humidity levels below 30% may lead to respiratory problems, excessive dryness, and potential harm to furniture and vegetation.[21] Therefore, regulating relative humidity (%RH) within the optimal range of 45–55% is essential to ensure a comfortable and health-supportive indoor environment.[22] Nevertheless, current humidity sensors often struggle with limitations in accuracy, response speed, and long-term reliability. To address these issues, researchers are actively investigating advanced sensing materials, innovative structural designs, and emerging technologies to create humidity sensors with enhanced sensitivity, selectivity, responsiveness, and stability for diverse applications. In this context, multifunctional materials that exhibit excellent electrochemical

[a]Department of Chemistry, Manipal Institute of Technology, Manipal Academy of Higher Education, Manipal 576104, Karnataka, India. E-mail: selva.kumar@manipal.edu

[b]Department of Physics, Manipal Institute of Technology, Manipal Academy of Higher Education, Manipal 576104, Karnataka, India

[c]Department of Humanities and Management, Manipal Institute of Technology, Manipal Academy of Higher Education, Manipal, 576104, Karnataka, India

[d]CSIR - Central Institute of Mining and Fuel Research (CIMFR), Digwadih Campus, PO:FRI, Dhanbad-828108, Jharkhand, India

performance along with responsive sensing capabilities are of particular interest. Such materials can serve as active electrodes in MSCs while also responding to external changes, such as humidity, through detectable variations in their electrical resistance. This dual functionality arises from the inherent properties of the material, such as high surface area (*e.g.*, MWCNTs), redox-active sites (*e.g.*, SnTe), tunable conductivity, and structural flexibility, all of which contribute to both efficient charge storage and high sensitivity to environmental stimuli. Tin-based chalcogenides,[23–25] particularly tin telluride (SnTe), are emerging as promising candidates for supercapacitor applications due to their advantageous electrochemical and structural properties.[26,27] The primary challenge with Sn-based electrodes stems from mechanical instability caused by significant volume expansion during cycling, which leads to poor structural integrity, reduced flexibility, and cluster formation. To address these issues, researchers have focused on engineering Sn-based materials with structural modifications. Reports on SnTe are limited, showing only moderate energy and power densities, though its rock-salt structure, narrow bandgap, and layered configuration favour high conductivity, ion intercalation, and pseudocapacitance.[28] Despite progress, conventional SnTe synthesis methods remain complex and often inconsistent. Thiol-free precursors yield nanocrystals but suffer from scalability issues,[29] while aqueous hot-injection improves sustainability yet lacks reproducibility.[25] One-pot aqueous synthesis enables gram-scale production but compromises uniformity and crystallinity.[28,30] To address these challenges, this work introduces the first assisted synthesis of multifunctional polycrystalline SnTe unwrapped MWCNT (SUM) crystal-based nanocomposites using a Bridgman-type crystal puller method. By integrating the high pseudocapacitance of SnTe with the excellent conductivity, flexibility, and structural stability of MWCNTs, the SUM composite functions as a dual-role material for both flexible microsupercapacitors (MSCs) and real-time humidity sensors. A SnTe/MWCNT humidity microsensor was integrated into a wireless prototype based on an ESP-32 microcontroller, enabling continuous resistance monitoring with rapid signal processing and low-latency data transmission for applications in wearable devices, IoT systems, and real-time crop monitoring *via* moisture detection on plant leaves. Electrochemical analyses confirmed high charge-storage capability, excellent bending stability, and durable energy storage performance of SnTe-MWCNT-based MSCs. Pristine SnTe is prone to nanoparticle agglomeration, which restricts ion/moisture diffusion and diminishes electrochemical activity.[31] Incorporating MWCNTs suppresses aggregation while providing a conductive porous network, thereby enhancing capacitance, flexibility, sensitivity, and response/recovery in humidity sensing. This multifunctional composite shows strong potential for next-generation integrated energy storage and environmental monitoring platforms. This work demonstrates the successful synthesis of a polycrystalline SnTe/MWCNT (SUM) nanocomposite *via* a Bridgman-type crystal puller-assisted strategy and its application in the fabrication of flexible microsupercapacitors (MSCs) and humidity sensors using screen-printing technology. The SUM nanocomposite synergistically integrates the high pseudocapacitance of SnTe with the conductivity, flexibility, and porous framework of MWCNTs, effectively overcoming the intrinsic limitations of pristine SnTe. The optimized asymmetric SUM-10 device delivered an impressive areal capacitance of 468.6 mF cm^{-2} at 5 mV s^{-1}, outstanding rate capability with capacitance retention of 96.8% (FAM) and 93.2% (FSM), and superior cycling stability, maintaining a coulombic efficiency of 98.7% over 5000 cycles under repeated bending. As a humidity sensor, SUM-10 exhibited rapid response (68 s) and recovery (162 s) times, high sensitivity, and stable performance even under mechanical deformation. Furthermore, a real-time monitoring prototype was realized using FDM 3D printing integrated with a microcontroller for continuous humidity tracking. Collectively, these results establish SUM-10 as a versatile dual-functional platform that combines high-performance energy storage with reliable environmental sensing, paving the way for next-generation wearable electronics, IoT devices, and precision agriculture applications.[32,33]

2. Materials and methods

2.1. Materials

The following chemicals were used in this study: tin metal (Sn), tellurium (Te), multi-walled carbon nanotubes (MWCNTs), cellulose acetate butyrate (CAB), diacetone alcohol ($C_6H_{12}O_2$), ethanol (C_2H_5OH), and methanol (CH_3OH), and the salts, such as LiCl, CH_3COOK, $MgCl_2$, K_2CO_3, $(MgNO_3)_2$, $CuCl_2$, NaCl, KCl, KNO_3, and K_2SO_4 required for the humidity sensing application, were all supplied by LOBA Chemie PVT. Ltd. All chemicals were of analytical grade and purchased from Sigma Aldrich with a stated purity of 99.9%.

2.2. Preparation of polycrystalline SnTe and SnTe/MWCNT (SUM) functional nanocomposites

The synthesis of SUMs as a functional material was carried out using the crystal growth method to obtain high-purity polycrystalline SnTe with superior crystallinity. A Bridgman-type crystal puller setup was employed for the growth process, specifically designed to produce high-quality SnTe crystals doped with multi-walled carbon nanotubes (MWCNTs).[29,34] Initially, tin (Sn) and tellurium (Te) powders were mixed in a stoichiometric ratio and thoroughly homogenized. The resulting mixture, along with a pre-determined amount of MWCNTs, was loaded into a quartz ampoule. The ampoule was then evacuated to a high vacuum ($\sim 10^{-5}$ torr) and sealed to prevent oxidation during the synthesis process. The sealed ampoule was subjected to a controlled heating cycle in the Bridgman furnace to promote crystal growth and ensure uniform incorporation of MWCNTs into the SnTe matrix. The ampoule was sealed and subjected to a molten growth process by heating it to 700 °C in a furnace. The temperature was maintained for 12 h to ensure complete melting and crystallization of SnTe. Subsequently, the ampoule was cooled to room temperature at a controlled rate, promoting the formation of polycrystalline SnTe with high crystalline quality. To enhance

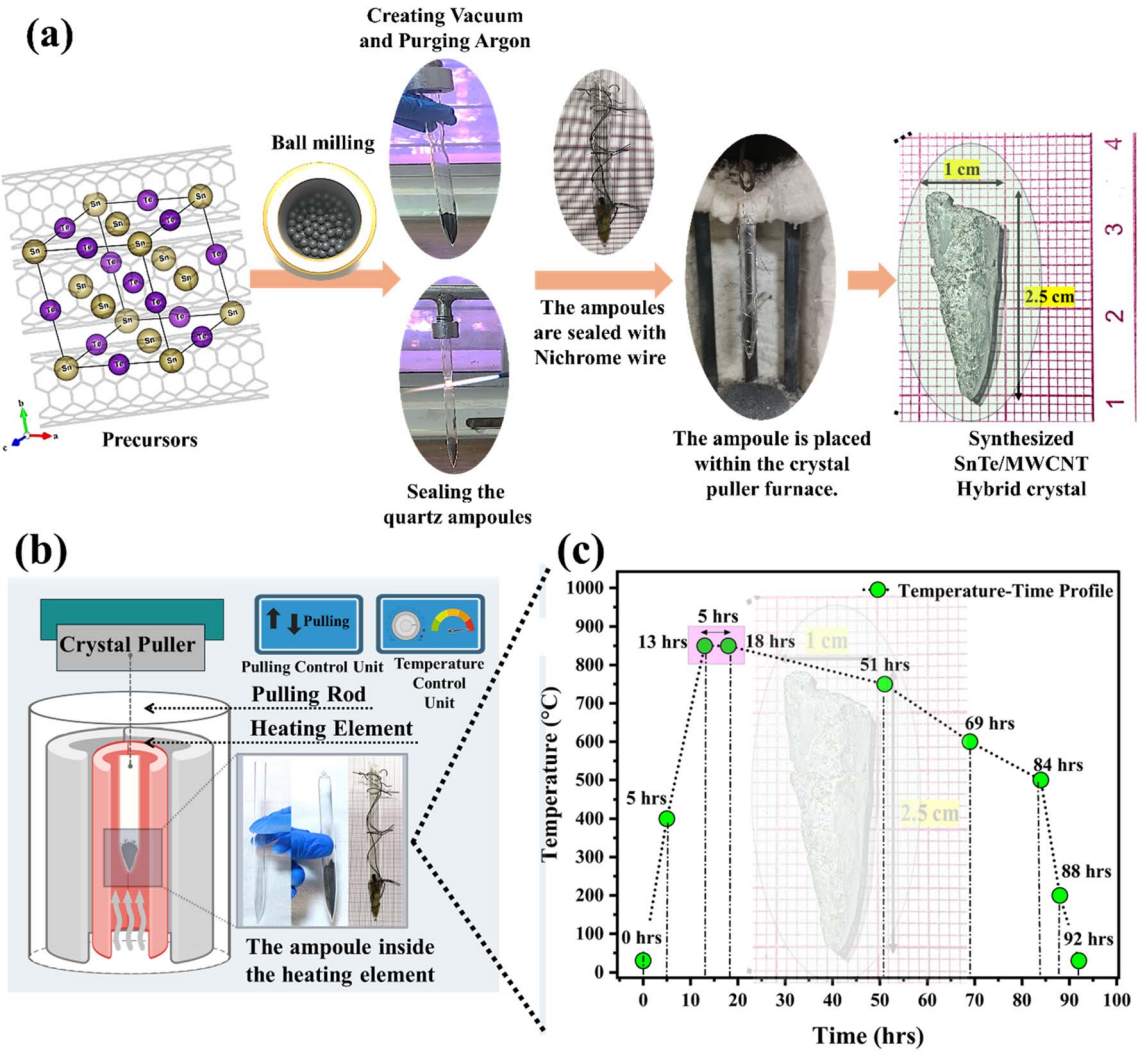

Scheme 1 (a–c) Synthesis and growth of MWCNT-wrapped SnTe crystals *via* the Bridgman molten-crystal method (1 cm, 2.5 cm). The process involved ball milling of precursors, vacuum sealing in quartz ampoules, and controlled crystallization to obtain the SnTe/MWCNT hybrid crystal. (a) Experimental setup of the Bridgman furnace, (b) pulling control unit equipped with precise temperature regulation (°C), and (c) progressive growth of the MWCNT-doped SnTe ingot using the Bridgman configuration, showing the optimized temperature–time profile for uniform crystal formation.

the uniformity of the nanocomposite, MWCNTs were pre-treated by ultrasonication in ethanol to reduce the agglomeration and improve their distribution. The dried MWCNTs were then mechanically mixed with Sn and Te precursors prior to synthesis to obtain a homogeneous nanocomposite structure suitable for advanced energy storage applications. The pristine SnTe polycrystal was synthesised using the approach without the incorporation of the MWCNTs. Furthermore, nanocomposites were synthesized by varying the weight percentage of MWCNTs relative to the SnTe content in the reaction mixture. Specifically, compositions containing 3 wt%, 5 wt%, 10 wt%, and 15 wt% MWCNTs were prepared to investigate the influence of MWCNT loading on the structural and functional properties of the resulting SnTe/MWCNT polycrystal-based nanocomposites, as summarized in Table S1. The synthesized bulk nanocomposite was subsequently crushed into a fine powder using a high-energy ball milling process to reduce the particle size to the nanoscale. The milling was performed at 300 rpm for 6 h under an inert argon atmosphere to prevent oxidation and maintain the material's integrity and purity. Scheme 1(a) demonstrates the process of the SnTe/MWCNT crystals *via* the Bridgman crystal growth method, involving ball milling, vacuum-sealed quartz ampoules, and crystal growth in a Bridgman crystal puller.

2.3. Mechanism for the synthesis of the SnTe/MWCNT hybrid crystal

Scheme 1(b) and (c) depict the synthesis procedure of the SnTe/MWCNT hybrid crystal. The mechanism involves a combination of thermally driven chemical reactions and physical interactions between the SnTe matrix and multi-walled carbon nanotubes (MWCNTs). During the high-temperature reaction processing under a vacuum, Sn and Te precursors react to form

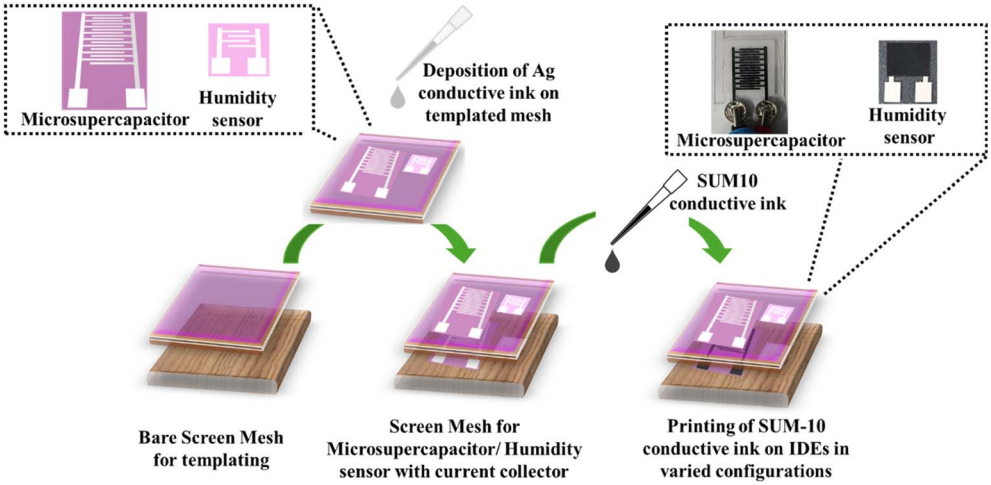

Scheme 2 Schematic representation of the fabrication process of microsupercapacitors and humidity sensors using a screen-printing approach.

a homogeneous molten SnTe phase. Owing to their high thermal stability, the dispersed MWCNTs remain structurally intact within the melts and act as heterogeneous nucleation center for SnTe crystallization.[35] Due to the interfacial interactions, primarily governed by the van der Waals force of interaction between the graphitic walls of MWCNTs and SnTe species, SnTe preferentially nucleates and grows along the nanotube surfaces,[36] as shown in Scheme 1(a).[37,38] Furthermore, the directional solidification in the Bridgman configuration promotes the controlled crystal growth along the temperature gradient. This process facilitates the incorporation of MWCNTs into the SnTe matrix, leading to a nanocomposite structure in which MWCNTs are embedded or encapsulated within the SnTe grains, enhancing the electrical and thermal transport properties of the final ingot. The temperature–time profile of the reaction was designed with stepwise increments to prevent unwanted cracking and to promote uniform crystal growth, as shown in Scheme 1(b). Furthermore, the schematic depicts SnTe nanoparticles embedded within the tubular MWCNT framework through van der Waals interactions, demonstrating homogeneous dispersion and intimate interfacial contact. Such a well-integrated heterostructure is essential for improving charge transport, accelerating both ion diffusion and thereby enhancing the overall electrochemical performance of the nanocomposite.

2.4. Formulation of the functional conductive ink for the microsupercapacitor and micro-humidity sensor

The formulation of functional conductive ink was prepared by dispersing the synthesized nanocomposite into an eco-friendly binder solution. The binder was formulated by dissolving cellulose acetate butyrate (CAB) in a solvent mixture of ethanol and diacetone alcohol using probe sonication at high frequency to form a homogeneous vehicle resin, maintaining a solvent-to-binder ratio of 90 : 10 to ensure optimal rheological behaviour for screen printable inks. To enhance dispersion stability, a non-ionic surfactant (Triton X-100) was added to the binder solution. The nanocomposite was incorporated into the binder solution and stirred vigorously for 2 h, followed by sonication for an additional 1 h at room temperature to ensure homogeneous dispersion and minimize agglomeration. The ink's viscosity was fine-tuned by adjusting the binder concentration to ensure optimal printability, with the final viscosity ranging between 2000 and 10 000 mPa s, depending on the shear rate and temperature. The formulated ink exhibited thixotropic behaviour, which facilitated smooth passage through the screen mesh during printing while maintaining excellent adhesion to flexible substrates such as polyethylene terephthalate (PET). This ink was used for fabricating interdigitated microsupercapacitors and micro-humidity sensors using the screen-printing method, as illustrated in Scheme 2. The preparation of a screen mesh with an interdigitated pattern using the negative-positive technique involves numerous processes to create a precise stencil for the screen-printing method. In screen printing, a positive process involves hardening the emulsion in areas corresponding to the design so that ink is blocked in those regions, whereas a negative process involves blocking off the inverse of the design, allowing ink to pass through the desired pattern. The entire stepwise protocol is illustrated in SI Scheme S1 (from the bare screen to a fully fabricated customized screen mesh for flexible microsupercapacitor and humidity sensor templates), as shown in Scheme S1.

2.5. Fabrication of flexible printed interdigitated devices

The fabrication of the microsupercapacitor and micro-humidity sensor was carried out using screen printing technology on a polyethylene terephthalate (PET) substrate (135 ± 5 μm), utilizing a formulated conductive functional ink. The printing process involved the initial deposition of the current collector (Ag current collector), which serves as the first conductive layer and the electrical connection for the device. This was followed by the printing of the active functional material in multiple layers, with the number of layers varied and optimized for

enhanced performance. After printing, the device was baked at 70–80 °C for one hour to ensure the evaporation of excess solvents from the printed functional matrix. This post-processing step is critical as it facilitates strong adhesion between the printed layers and the PET substrate. As a result, the device maintains excellent mechanical flexibility and stable electrochemical performance, even after repeated bending cycles, without any significant loss in functionality. The fabricated microsupercapacitors have overall dimensions of 22.9 × 13.6 mm (length × breadth) and consist of 16 interdigitated electrodes (IDEs), which enhance ionic mobility and increase the effective surface area at the electrode/electrolyte interface. In contrast, the micro-humidity sensor features a surface area of 10.5 × 7.9 mm and incorporates two pairs of IDEs, each with a thickness of 0.5 mm. Furthermore, the effect of overprinting (OP) of both the IDEs and the sensing layer has also been evaluated to understand its influence on device performance. Scheme S2 illustrates the overall printing strategy and matrix layout of the fabricated devices. Electrodes were prepared by the conventional slurry deposition method using *N*-methyl-2-pyrrolidone (NMP) as the solvent and polyvinylidene fluoride (PVDF) as the binder. The active material and acetylene black were dispersed in NMP/PVDF to form a homogeneous slurry, which was blade-coated onto stainless steel current collectors (1 × 1 cm^2). After drying under controlled conditions, the electrodes were tested using a Biologic SP-50e workstation in a three-electrode setup with Pt counter and saturated calomel reference electrodes. Cyclic voltammetry (CV) and electrochemical impedance spectroscopy (EIS) were used to evaluate capacitive and charge-transfer characteristics. Humidity response and recovery were analysed in a customized chamber across 11–97% RH.[39–47]

3. Results and discussion

3.1. XRD analysis

The X-ray diffraction (XRD) analysis, as illustrated in Fig. 1, reveals insights into the crystalline structure and phase composition of pristine SnTe, pristine multi-walled carbon nanotubes (MWCNTs), and their nanocomposites named SUM-3, SUM-5, SUM-10, and SUM-15. Fig. 1(a) shows the XRD pattern of pristine SnTe, exhibiting sharp and well-defined peaks at 2θ values of 27.9°, 41.2°, 50.8°, 66.0°, 73.1°, and 77.5°, corresponding to the (200), (220), (222), (400), (420), and (422) planes, respectively, which are indexed to the face-centered cubic (FCC) phase with $Fm\bar{3}m$ of SnTe (JCPDS card no 08-0487). This confirms the formation of highly crystalline and phase-pure SnTe.[28,34,48] In contrast, Fig. 1(a) shows pristine MWCNTs displaying a broad peak centred at 25.6°, attributed to the (002) reflection of graphitized carbon present within the interconnected tubular structure. Upon incorporation of MWCNTs into SnTe, all characteristic peaks of SnTe are retained in the SUM-series nanocomposites, indicating the preservation of its polycrystalline structure post-hybridization. Notably, a gradual increase in the intensity and sharpness of the slightly broadened MWCNT (002) hump is observed with higher MWCNT content, particularly in SUM-10 and SUM-15, confirming successful integration and increased carbon content. Fig. 1(b) shows a zoomed-in region highlighting the (200) and (220) phases between 27.9° and 40.2°. The SUM nanocomposites retain the SnTe major characteristic peaks, but with a notable leftward shift in peak positions, especially in the (200) and (220) planes, as magnified in Fig. 1(c). This systematic shift towards lower 2θ angles suggests lattice expansion or tensile strain, likely due to the incorporation of carbon nanotubes into the SnTe matrix, leading to slight distortions in the crystal lattice and modification of the interplanar spacing. Such a shift can also arise from interfacial stress between the SnTe grains and the embedded MWCNTs, as well as the quantum confinement effect at the nanoscale. Furthermore, a broad graphitic hump centred at 22.0°, marked with an asterisk (*) in the combined diffraction pattern shown in Fig. 1(d), is observed exclusively in nanocomposites with higher graphitic carbon content (*i.e.*, SUM-10 and SUM-15). This feature is characteristic of the amorphous or turbostratic graphitic structure associated with MWCNTs and validates their successful incorporation into the composite matrix at higher concentrations. Additionally, Rietveld refinement was performed using FullProf software© to analyse the structural characteristics of the synthesised pristine SnTe polycrystal. As illustrated in Fig. 1(e), the refinement exhibits excellent fitting quality, as evidenced by low residual values ($\chi^2 = 1.70$), confirming the high phase purity and structural stability of the synthesized SnTe without detectable secondary phases. The average crystallite size of the nanocomposite increases with the addition of MWCNTs, reaching a maximum of 28.1 nm at SUM-10. This suggests that the inclusion of CNTs facilitates better crystalline ordering and growth. Among all compositions, the SUM-10 nanocomposite shows the optimal crystallite size, indicating superior structural quality. This enhancement can be attributed to the well-dispersed MWCNTs serving as nucleation centres and promoting uniform crystal growth.[49,50] At higher loading (15 wt%), a slight reduction in crystallite size is observed, possibly due to agglomeration of MWCNTs, which can hinder crystallite formation. Therefore, 10 wt% MWCNTs is identified as the optimal composition for achieving improved structural and functional properties. The enhancement in crystallite size with 10 wt% MWCNT addition corresponds to improved crystalline order and stronger interfacial interaction between the matrix and the conductive additive. This structural optimization results in superior performance by providing enhanced electron mobility, improved ion diffusion pathways, and lower charge transfer resistance. Hence, SUM-10 demonstrates the best balance between structural and functional properties such as lower interfacial resistance and enhanced interaction between the functional nanocomposites and the active surface, making it the optimal composition for the fabrication of electrodes as well as for high-performance sensing applications.[51] The crystallite size of the synthesized nanocomposites was estimated by analysing the broadening of the diffraction peaks in the corresponding XRD patterns. The quantitative evaluation was carried out using the Scherrer equation, as expressed in eqn (1).

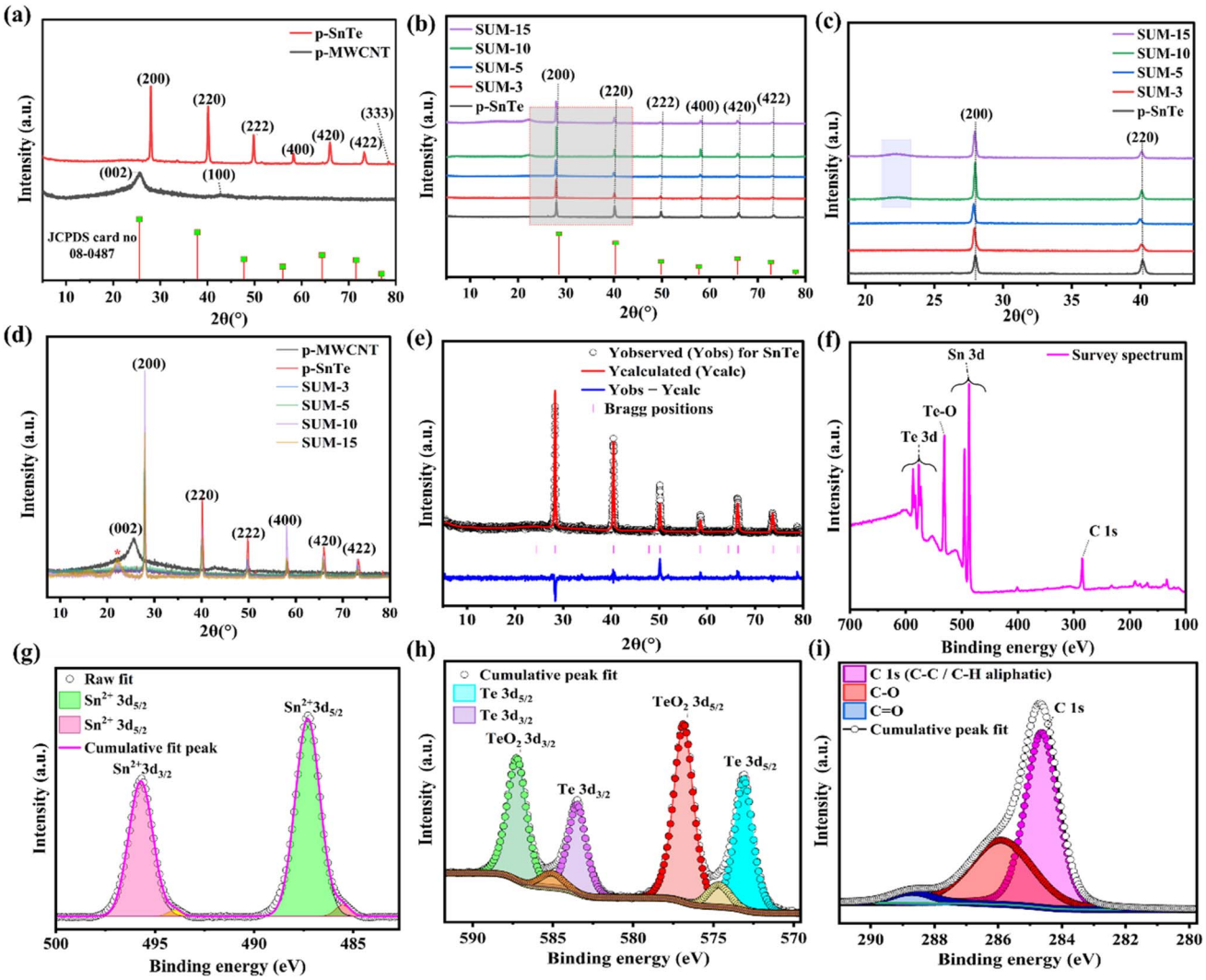

Fig. 1 (a)–(i) The XRD patterns of pristine SnTe, MWCNTs, and SnTe-based nanocomposites (SUM-3, SUM-5, SUM-10, and SUM-15), (a) comparison of p-SnTe and p-MWCNT, (b) the evolution of diffraction peaks with MWCNT concentrations, (c) the shift and broadening of the (200) and (220) peaks, (d) overlay of all samples for phase comparison, and (e) the Rietveld refinement confirming phase purity and fitting accuracy. (f) Survey spectrum confirming the presence of Sn, Te, and C elements; (g) high-resolution Sn 3d spectrum, (h) deconvoluted Te 3d spectrum, and (i) C 1s spectrum.

$$D = \frac{K\lambda}{\beta \cos(\theta)} \quad (1)$$

Furthermore, the structural parameters derived from the XRD analysis reveal a strong correlation between CNT content and the microstructure within the SnTe-based nanocomposites. As the concentration of MWCNTs increases from 3 wt% to 10 wt%, the crystallite size increases from 25.8 nm (SUM-3) to a maximum of 29.06 nm (SUM-10), as tabulated in Table S2. This growth suggests that MWCNTs act as nucleation templates, facilitating grain development and improved crystallinity within the matrix. However, beyond 10 wt% (SUM-15), the crystallite size slightly decreases to 28.0 nm, likely due to the onset of nanotube agglomeration, which hinders uniform crystal growth. This observation is supported by the dislocation density (δ) and microstrain (ε) values, both of which increase progressively with MWCNT concentration, peaking at SUM-15. While a moderate increase in microstrain and dislocation density (as seen in SUM-10) can introduce beneficial defects that enhance electrochemical reactivity by providing more active sites, the excessively high defect levels in SUM-15 may result in charge recombination centres and structural instability due to the intertwining of the CNTs. Thus, the SUM-10 nanocomposites achieve an optimal balance between crystallite size, structural defects, and strain, which is expected to enhance electron transport and ion diffusion, which act as key factors for superior electrochemical performance.

3.2. XPS (X-ray photoelectron spectroscopy) analysis

XPS analysis provides detailed insight into the elemental composition and chemical states of the SnTe nanocomposite. The survey spectrum shown in Fig. 1(f) confirms the presence of

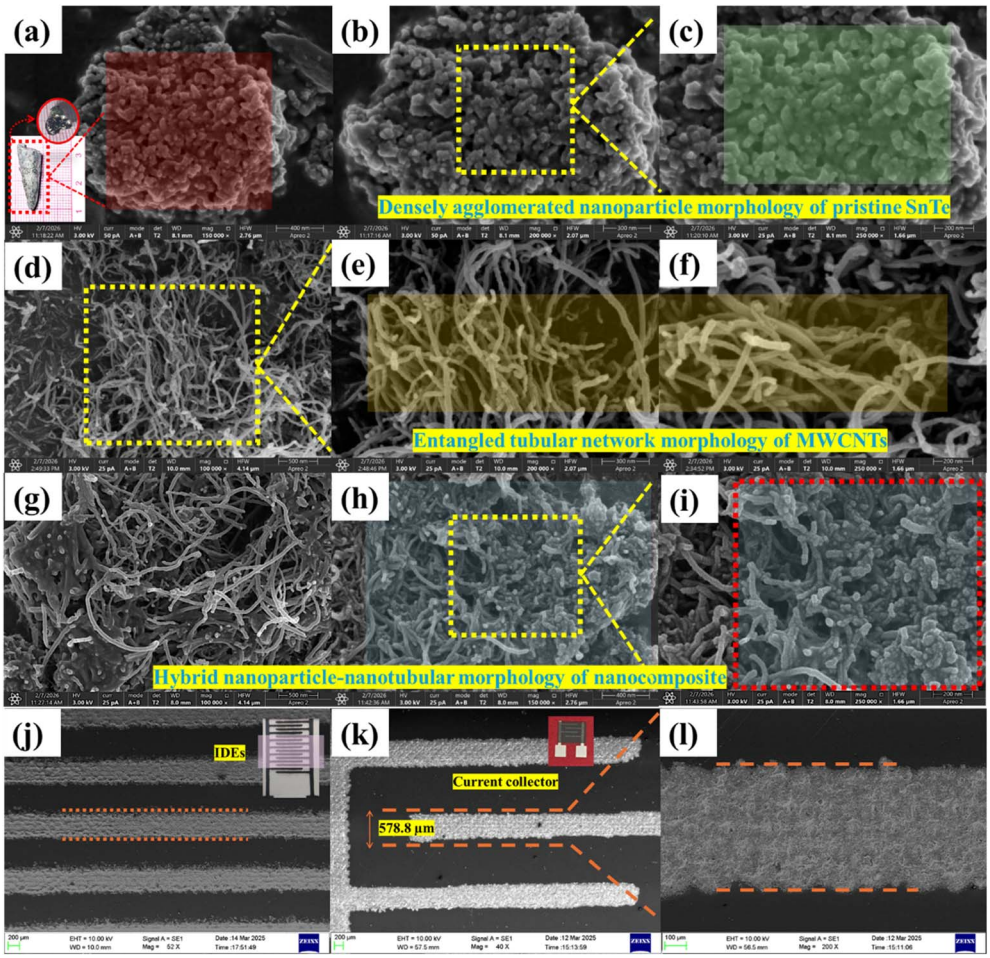

Fig. 2 FESEM micrographs showing (a)–(c) pristine polycrystalline SnTe with agglomerated nanoparticles morphology, (d)–(f) pristine MWCNTs exhibiting a tubular network, (g)–(i) SnTe/MWCNT nanocomposite showing an integrated nanoparticle–nanotubular architecture, and (j)–(l) screen-printed interdigitated electrode (IDE) pattern fabricated using the nanocomposite ink.

key elements, including tin (Sn), tellurium (Te), and carbon (C), with distinct peaks observed for Sn 3d, Te 3d, and C 1s. A Te–O signal is also detected, which is attributed to surface oxidation as expected from the surface-sensitive nature of XPS measurements.[52] High-resolution spectra further elucidate the chemical states of these elements. In Fig. 1(g), the Sn 3d spectrum reveals two prominent peaks corresponding to the spin–orbit doublets Sn $3d_{5/2}$ and Sn $3d_{3/2}$ at binding energies of approximately 486.5 eV and 495.0 eV, respectively. These values are characteristic of Sn^{2+} oxidation states, indicating the presence of divalent tin species in the sample. Fig. 1(h) presents the deconvoluted Te 3d spectrum, where two main peaks at ~573.1 eV and ~583.5 eV correspond to Te $3d_{5/2}$ and Te $3d_{3/2}$, respectively. These binding energies are characteristic of Te^{2-} species in the SnTe lattice, confirming the formation of the SnTe phase. In addition, a secondary doublet observed at higher binding energies of 576.8 and 587.3 eV is attributed to Te^{4+} species (TeO_2), indicating mild surface oxidation arising from ambient exposure.[53,54] Additionally, the C 1s spectrum in Fig. 1(i) reveals contributions from different carbon bonding environments. The main peak at ~284.6 eV corresponds to aliphatic C–C/C–H bonds, while the minor peaks at higher binding energies indicate the presence of C–O and C=O functionalities,[55] likely originating from surface-adsorbed organic species or residual solvents. Overall, the XPS results validate the successful synthesis of the SnTe nanocomposite with Sn^{2+} and Te^{2-} oxidation states, while the surface chemistry shows minor contamination from carbonaceous species.[29]

3.3. Field emission scanning electron microscopy (FESEM) analysis

FESEM analysis was performed to examine the morphology, size distribution, and surface features of the pristine material and synthesized nanocomposites (Fig. 2(a)–(i)). High-resolution imaging provides crucial insights for electrochemical energy storage and sensing applications, revealing microstructural traits that impact surface area, particle distribution, and interfacial interactions, all of which influence device performance. For SnTe/MWCNT nanocomposites, FESEM analysis confirms uniform material distribution, evaluates nanoparticle and CNT agglomeration, and assesses interfacial bonding. When combined with EDX spectroscopy, it also provides elemental

composition and mapping. The FESEM micrographs of pristine polycrystalline SnTe nanoparticles, as shown in Fig. 2(a)–(c), reveal a densely agglomerated nanoparticle morphology with notable size heterogeneity and extensive particle clustering, as evident from the micrographs. Their spherical morphology promotes better interfacial contact with carbon-based materials, increasing surface area and ion accessibility, thereby improving electrochemical performance. Additionally, pristine MWCNTs, as shown in Fig. 2(d)–(f), clearly exhibit the morphology of interconnected nanotubes, forming a porous and entangled network. This structure facilitates efficient electron transport and provides a large surface area, which is beneficial for enhancing electrochemical performance in energy storage and sensing applications. The formation of the SUM-10 nanocomposite is shown in Fig. 2(g)–(i), illustrating the development of an integrated SnTe/MWCNT hybrid structure. Upon completion of the reaction, SnTe nanoparticles are uniformly distributed within the interconnected MWCNT network, with minor localized clustering. The MWCNTs preserve their tubular morphology, serving as a conductive scaffold, while partially wrapping around SnTe nanoparticles to improve the dispersion, suppress excessive agglomeration, and improve interfacial contact. This structural integration promotes a synergistic effect, combining efficient electron transport through the carbon framework and electrochemically active sites provided by dispersed SnTe nanoparticles, thereby contributing to improved composite performance.[56] The advanced nanocomposite in Fig. 2(i) demonstrates the successful formation of the desired hybrid morphology, with SnTe nanoparticles intimately integrated within the MWCNT (SUM) network. This 3D conductive framework ensures uniform active material distribution, mechanical stability, efficient electron transport, and accessible SnTe surfaces for electrochemical reactions.[57] The fabricated interdigitated electrodes (IDEs) on flexible PET substrates exhibit precise geometry and high surface quality. Both the microsupercapacitor and humidity sensor IDEs have a uniform spacing of 0.5 mm ± 0.1 mm (Fig. 2(j)–(l)), with clearly defined deposition of the silver current collector and SUM electrode material. The current collector shows a consistent thickness of ~578.8 μm (~0.57 mm) (Fig. 2(k)), ensuring reliable electrochemical and sensing performance. This IDE design reduces ion diffusion paths, enhances electric field strength, and improves device response, with FESEM confirming the accurate achievement of the intended electrode geometry. The FESEM analysis highlights structural features critical for device performance. In microsupercapacitors, the SnTe/MWCNT nanocomposite provides a high surface area, excellent conductivity, efficient charge transfer, and mechanical stability, preventing material detachment during cycling. For humidity sensors, the screen-printed porous sensing layer enables effective moisture adsorption, while the MWCNT network ensures rapid signal transmission and stable electrical response and recovery.

3.4. Transmission electron microscopy (HRTEM) analysis

HRTEM analysis was conducted to investigate the structural characteristics and morphological features of the SUM nanocomposites in more detail (Fig. 3(a)–(f)). The micrograph revealed distinct structural components, including SnTe nanoparticles and carbon nanotube elements within the composite system. The micrograph demonstrates the presence of SnTe nanoparticles displaying characteristic particle morphology

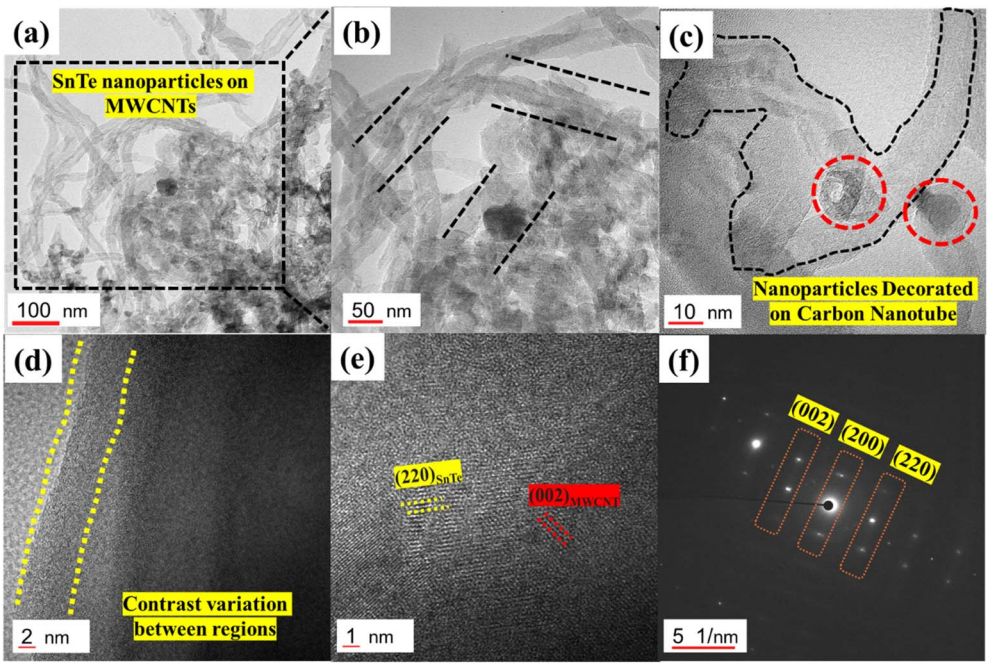

Fig. 3 (a)–(f) HRTEM analysis of the SnTe/MWCNT nanocomposite showing (a) and (b) low-magnification TEM images of SnTe nanoparticles anchored onto MWCNTs, (c) and (d) high-resolution images displaying lattice fringes of crystalline SnTe and graphitic carbon walls, and (e) atomic-scale lattice fringes corresponding to the (220) plane, and (f) SAED pattern with indexed (002), (200), and (220) reflections.

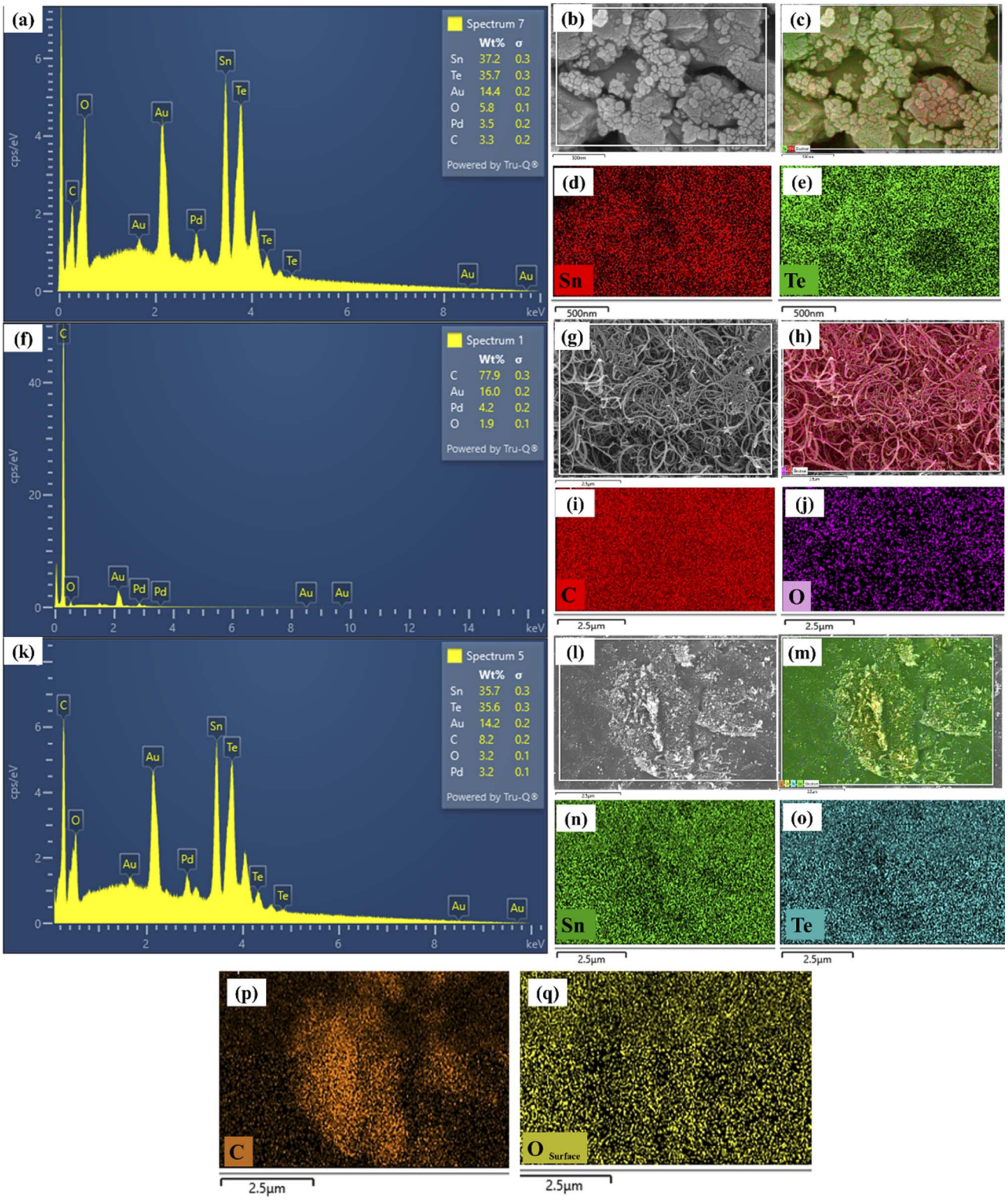

Fig. 4 Elemental mapping and EDX analysis of (a–e) SnTe nanoparticles: (a) EDX spectrum, (b) FESEM image, (c) overlay map, and (d and e) Sn and Te maps; (f–j) MWCNTs: (f) EDX spectrum, (g) FESEM image, (h) overlay map, and (i and j) C and O maps; and (k–q) SnTe-MWCNT nanocomposite: (k) EDX spectrum, (l) FESEM image, (m) overlay map, and (n–q) Sn, Te, C, and O maps.

with well-defined crystalline boundaries (Fig. 3(a)). The nanotube structures shown in Fig. 3(b) reveal tubular morphologies consistent with multi-walled carbon nanotube characteristics. The higher magnification image (Fig. 3(c)) further reveals that the SnTe nanoparticles are intimately attached to the carbon nanotube surface, indicating strong interfacial contact between

the two components. This close interaction is essential for efficient charge transfer across the heterointerface. Fig. 3(d) displays contrast variations between regions, as indicated by the parallel dashed lines marking the crystalline nanoparticle domains and the graphitic nanotube walls. In Fig. 3(e), well-defined lattice fringes are observed with an interplanar spacing corresponding to the (200) plane of SnTe, while a lattice spacing of ~0.35 nm corresponds to the (002) plane of MWCNTs, characteristic of graphitic carbon. Furthermore, the selected area electron diffraction (SAED) pattern, as shown in Fig. 3(f), shows well-defined reflections corresponding to both SnTe and MWCNT phases in nanocomposites. The reflections at *d*-spacings of 0.32 nm and 0.22 nm correspond to the (200) and (220) crystallographic planes of SnTe, respectively, confirming the face-centred cubic structure. The reflection at 0.35 nm corresponds to the (002) graphitic interlayer spacing of MWCNTs, confirming the successful incorporation of carbon nanotubes in the nanocomposite system. This value aligns perfectly with the typical interlayer distance of 0.34–0.36 nm reported for multi-walled carbon nanotubes,[58] confirming the preservation of the graphitic structure during the composite synthesis process. The nanocomposite architecture demonstrates intimate contact between SnTe nanoparticles and carbon nanotube components, with the nanotube configuration potentially enhancing interfacial contact and charge transfer mechanisms. The hierarchical structure progression from the microscale to the atomic scale reveals a well-organized composite system with clean, well-defined interfaces and minimal amorphous regions. The nanocomposite exhibits strong interfacial interactions, mechanical stability, and high crystalline quality, promoting efficient charge transfer and favourable electronic transport. The well-structured SnTe nanoparticles integrated with MWCNTs create a synergistic effect, making the material suitable for advanced micro-supercapacitor and energy conversion applications.

3.5. Energy dispersive X-ray spectroscopy (EDX) analysis

EDX analysis was conducted to investigate the elemental composition and spatial distribution of elements within the pristine as well as SnTe-MWCNT nanocomposite system. The comprehensive elemental mapping provides crucial insights into the chemical composition, phase distribution, and homogeneity of the synthesized nanocomposite materials. The elemental mapping results demonstrate excellent spatial resolution and clearly distinguish the distribution of constituent elements throughout the nanocomposite structure. Fig. 4(a)–(e) present the EDS spectrum and corresponding elemental maps of pristine SnTe nanoparticles. The EDS analysis confirms the presence of the core elements Sn (37.2 wt%) and Te (35.7%), which are present in an approximately 1 : 1 ratio consistent with the stoichiometric composition of SnTe. A small amount of surface oxygen (5.8 wt%) is also detected, which may arise from the surface oxidation. The detected Au and Pd signals originate from the sputter coating during sample preparation, while the carbon signal is attributed to the conductive carbon tape used for mounting beneath the sample. The elemental maps further illustrate the spatial distribution of Sn and Te.The Sn elemental map (green) exhibits a relatively uniform distribution with localized clustering, corresponding to the SnTe nanoparticle regions. Similarly, the Te map (magenta) closely overlaps with the Sn distribution, confirming homogeneous elemental distribution and supporting the formation of SnTe phase. Moreover, Fig. 4(f)–(j) show the EDS spectrum and elemental maps for the pristine MWCNTs. The spectrum is dominated by the strong carbon peak (77.9 wt%), confirming the graphitic nature of nanotubes, with a minor oxygen signal attributed to surface functionalities. The carbon maps reveal a uniform distribution across the entangled network, while the oxygen maps show a weak and dispersed presence, indicating limited surface oxidation. Furthermore, Fig. 4(k)–(q) show the EDS analysis for the SnTe/MWCNT nanocomposite. The spectrum confirms the presence of Sn and Te along with carbon, with an estimated MWCNT content of ~8.2 wt%, which is close to the nominal 10 wt% composition of the SUM-10 nanocomposite, thereby verifying the successful integration of SnTe within the MWCNT framework. The elemental maps show a homogeneous distribution of Sn and Te overlapping with the carbon network, indicating the uniform distribution of SnTe nanoparticles across the conductive nanotube matrix of MWCNTs. The correlation between elemental maps and STEM morphology confirms the successful synthesis of a well-integrated nanocomposite.

4. Rheological analysis

4.1. Viscosity analysis

The synthesized nanocomposite was used for the formulation of the functional conductive ink by utilizing the pigment (optimized nanocomposite (SUM-10)), eco-friendly binder, and non-ionic surfactant to formulate a screen printable functional ink for the printing of the flexible microsupercapacitor and humidity sensor using screen printing technology.[6,59,60] The formulated ink was further evaluated using rheological analysis (viscosity, shear rate, and thixotropic behaviour). The viscosity was analysed at varied temperatures from room temperature (25 °C to 35 °C and 45 °C), respectively, as shown in Fig. 5(a).[61–67] The formulated ink shows excellent printability, stability, and thixotropic behaviour. The calculated viscosity for the formulated ink is $\eta = 6229.3$ at 25 °C. The presence of the MWCNTs within the SUMs provides structural stability and enhanced adhesion over the flexible substrate. The "η" of the functional shows a decreasing trend as the temperature is increased from room temperature to 45 °C. Shear rate analysis was carried out for the formulated ink, as shown in Fig. 5(b), which provides comprehensive insights into the flow behaviour of the formulated conductive ink under various shear conditions. Rheological studies over shear rate range of 0–700 s^{-1} show that the ink exhibits pronounced shear-thinning behaviour across 25–45 °C. Maximum shear stress decreases with temperature, from 8000 mPa s at 25 °C to 6000 mPa s at 35 °C and 3500 mPa s at 45 °C, demonstrating temperature-dependent viscosity reduction that eases processing at higher temperatures. Shear rate dependency analysis reveals that the formulated ink maintains excellent

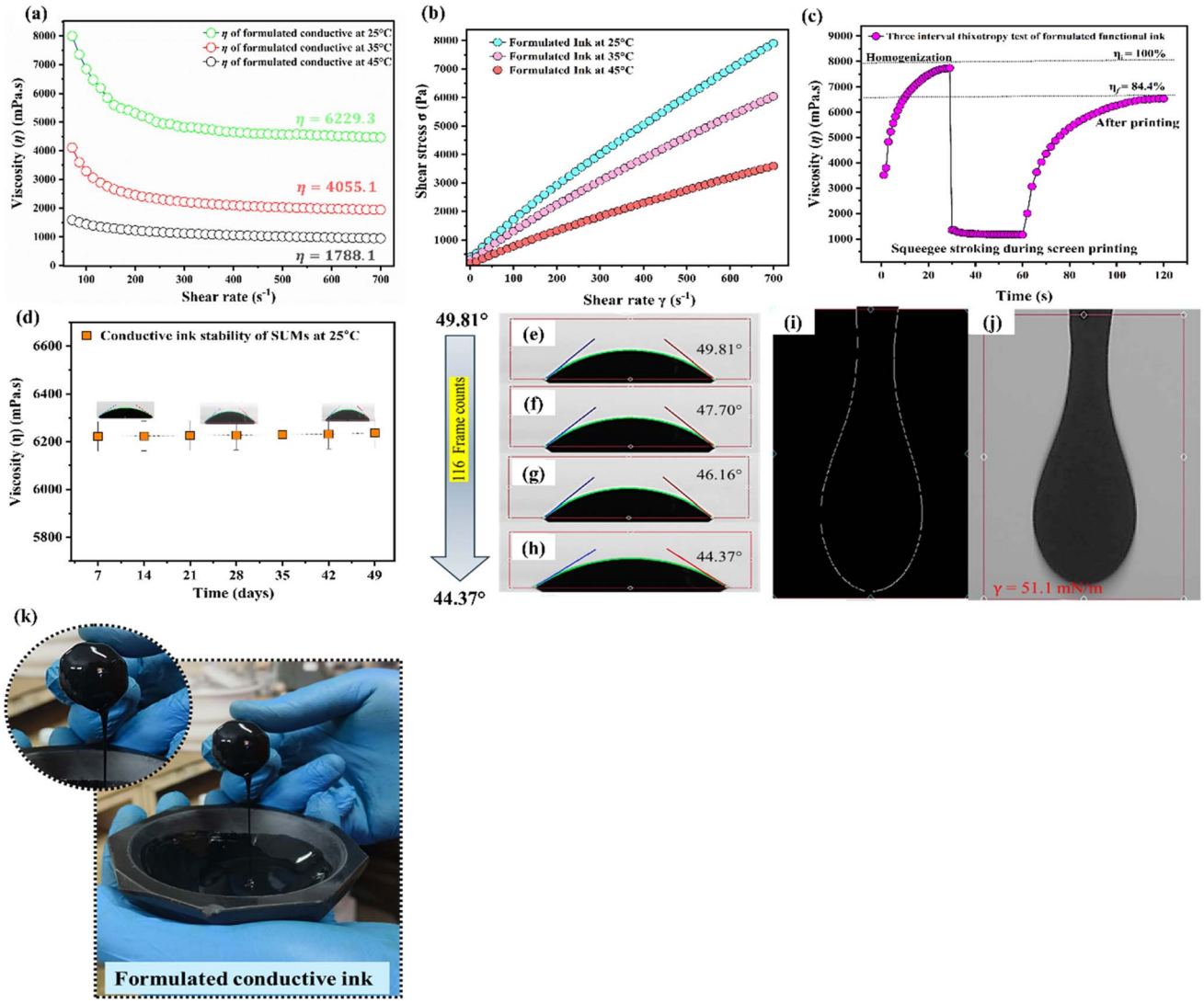

Fig. 5 (a–e) Show the rheological and stability profile of the formulated conductive ink. The ink exhibits shear-thinning behaviour (a) and pseudoplastic flow (b), while the thixotropy test (c) demonstrates structural recovery. Stable viscosity over time (d) confirms storage stability. Contact angle (e–h) and pendant drop analysis (i and j) indicate enhanced wettability and a surface tension of 51.1 mN m^{-1}, while (k) confirms uniform flow and homogeneity.

flow consistency throughout the entire shear rate spectrum, with no evidence of shear thickening or flow instabilities that could compromise printing quality. The typical shear rates range from 10 to 100 s^{-1} during ink transfer through screen mesh openings. The absence of yield stress behaviour at low shear rates suggests that the ink can initiate flow readily under minimal applied forces, which is advantageous for achieving uniform ink distribution across the screen surface and preventing clogging and incomplete transfer of the IDE pattern. The shear-thinning mechanism is primarily governed by the structural arrangement of SUMs and polymer chains within the ink matrix rather than temperature-induced molecular changes. This consistent shear-thinning profile ensures that the ink maintains optimal flow properties for screen printing applications, where it must flow smoothly under the applied squeegee pressure while rapidly recovering its structure to prevent post-printing deformation and maintain sharp edge definition in the printed patterns.[62,63] The three-interval thixotropic test (3ITT) behaviour was also analysed to understand the time-dependent viscosity over a time span of 120 s, which was categorized into three main subcategories: homogenization, interval during the stroking of the squeegee during printing, and after printing.[68] The recovery ratio, calculated using eqn (2) by comparing the initial viscosity (η_i) with the final viscosity (η_f), was found to be 84.4%.

$$\text{Recovery ratio} = \frac{\text{viscosity over time } (t)\ \eta_f}{\text{initial viscosity } \eta_i} \times 100 \qquad (2)$$

The formulated conductive ink exhibits excellent rheological stability and visual homogeneity as illustrated in Fig. 5(d)–(e). Viscosity monitoring over 49 days at 25 °C (Fig. 5(d)) shows

minimal variation, remaining consistently around 6200 mPa s. The results confirm the ink's long-term stability, essential for printed electronics, with contact angle measurements over time indicating consistent wettability and spreading, further validating the formulation's reliability during storage. Fig. 5(k) visually highlights the macroscopic behaviour of the ink during handling. The image captures the ink being poured, exhibiting a smooth, cohesive flow without fragmentation or phase separation. The uniform thread-like elongation reflects well-balanced viscoelastic properties, ensuring consistent ink transfer and precise patterning during device fabrication. The absence of agglomerates or sedimentation confirms dispersion homogeneity, indicating that the ink remains stable and ready for use in device assembly even after extended storage. Overall, these results demonstrate that the formulated ink preserves both structural integrity and functional printability, supporting reliable device performance over time.

4.2. Contact angle (°) and surface tension analysis (γ) of formulated ink

The contact angle and surface tension analysis were further conducted to evaluate the wettability and adhesion behaviour of the formulated functional ink on the flexible substrate. This analysis is crucial for determining the ink's compatibility with screen-printing processes and its ability to uniformly coat the substrate. The dynamic contact angle measurements were recorded over 116 frames at a frame rate of 30 frames per second (FPS), as illustrated in Fig. 5(e)–(h). The initial contact angle was observed at 49.81°, which progressively decreased to 44.37° by the 116th frame, indicating enhanced spreading of the ink droplet over time. This reduction in contact angle signifies improved wettability and strong interfacial adhesion of the ink to the substrate surface, which is essential for achieving defect-free, uniform printed films. The low contact angle ($\theta \approx 5.4°$) indicates optimized surface energy and good substrate compatibility, ensuring uniform film formation, consistent deposition, and strong adhesion, key to flexible device fabrication. Furthermore, the surface tension (γ) of the formulated ink was determined using the pendant drop method, as shown in Fig. 5i and j. By fitting the droplet profile to the Young–Laplace equation, the surface tension was calculated to be $\gamma = 51.1$ mN m^{-1}, a value within the ideal range for screen-printable inks (typically 30–60 mN m^{-1}). This moderately high surface tension ensures sufficient cohesion within the ink, while still allowing for effective wetting and spreading over the substrate. The droplet profile (Fig. 5(i)) and its analysis (Fig. 5(j)) confirm the ink's suitability for high-resolution, defect-free screen printing, validating its excellent interfacial properties for flexible printed electronics, including microsupercapacitors and sensors.

5. Electrochemical analysis

5.1. Electrochemical impedance (EIS) analysis

Electrochemical impedance spectroscopy (EIS) was employed to investigate the interfacial charge transport resistance and ionic conductivity of the fabricated electrodes, including the pristine samples (p-SnTe and p-MWCNT), their nanocomposites (SUM-3, SUM-5, SUM-10, and SUM-15), the flexible symmetric microsupercapacitor [FSM (SUM-10)], and the flexible asymmetric microsupercapacitor [FAM (SUM-10//Ac)], as illustrated in Fig. 6(a)–(d). In Fig. 6(a), the Nyquist plots for pristine SnTe and MWCNTs exhibit classic semicircles in the high-frequency region, followed by linear tails at low frequencies. The charge transfer resistance (R_{ct}), represented by the diameter of the semicircle, is markedly lower for MWCNTs than for SnTe, indicating improved electrical conductivity due to the conductive carbon network. Fig. 6(b) presents the Nyquist profiles of nanocomposites SUM-x (x = 3, 5, 10, and 15), which show a systematic decrease in R_{ct} up to SUM-10, followed by an increase in SUM-15. This trend reflects an optimal percolation threshold at SUM-10, beyond which excessive additive content leads to nanocluster agglomeration, increasing the resistance. The equivalent circuit fitting follows the $R(Q(R(Q(RW))))$ model, where R_s is the solution resistance, CPE is the constant phase element, and W is the Warburg impedance associated with ion diffusion. Notably, the screen-printed flexible device FSM(SUM-10) (Fig. 6(c)) displays a substantially lower R_{ct} than its drop-cast counterpart, confirming improved interfacial contact and homogeneous ink deposition. Furthermore, Fig. 6(d) shows that the hybrid architecture FAM(SUM-10//AC), containing activated carbon (AC), achieves the lowest R_{ct}, which is attributable to the high surface area and porous structure of AC, promoting electrolyte infiltration and rapid charge transfer.

5.2. Cyclic voltammetry (CV) analysis

The electrochemical behaviour and redox kinetics of the fabricated electrodes were further analysed using CV, as presented in Fig. 6(e)–(l). The comparative CV voltammogram curves of pristine SnTe and MWCNTs at 5 mV s^{-1} (Fig. 6(e)) show well-defined redox peaks at 0.37 V (cathodic) and 0.55 V (anodic), characteristic of faradaic charge storage, with a larger integrated area for MWCNTs, indicating higher areal capacitance. The areal capacitance (C_s) was calculated using the relationship (3):

$$C_A = \frac{\int I \mathrm{d}v}{vS\Delta V} \quad (3)$$

where "v" is the scan rate in (V s^{-1}). CV voltammograms of nanocomposites at varying scan rates from 5–100 mV s^{-1} are shown in Fig. 6(f)–(i). SUM-10 (Fig. 6(h)) shows the most symmetric redox peaks and stable area across scan rates, while SUM-15 (Fig. 6(i)) displays distorted shapes and reduced peak currents, signifying limited ion diffusion and charge storage due to increased internal resistance. A direct comparison at 5 mV s^{-1} (Fig. 6(j)) confirms that SUM-10 yields the highest current response and enclosed area, validating its superior electrochemical performance. The CV profiles of the printed devices FSM(SUM-10) (Fig. 6(k)) and FAM(SUM-10//AC) (Fig. 6(l)) show nearly rectangular curves with minor redox features, typical of electric double-layer capacitors (EDLCs). The FAM(SUM-10//AC) architecture delivers the highest current density and area, benefiting from the combination of faradaic

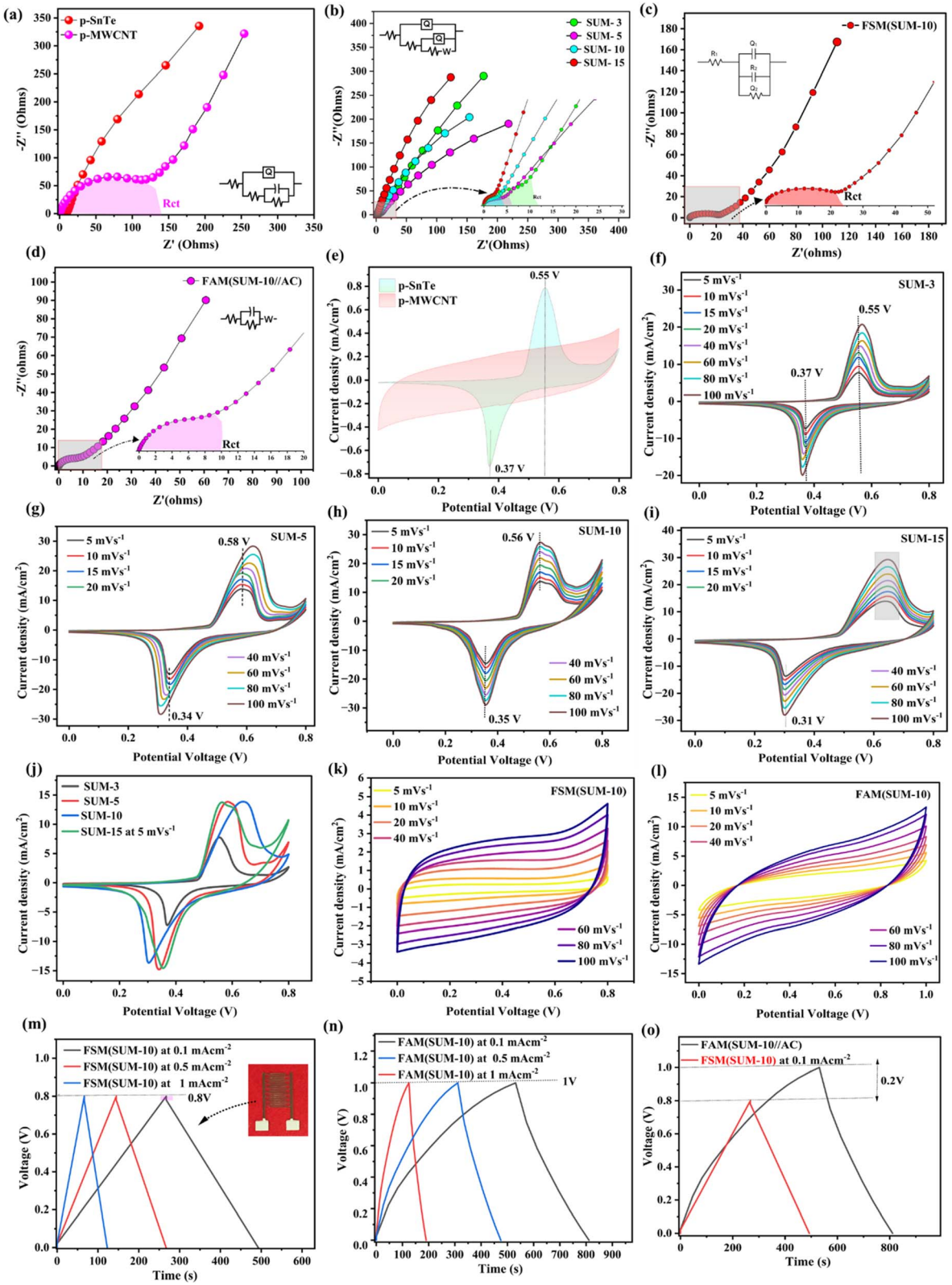

Fig. 6 (a)–(d) Nyquist plots for p-SnTe, p-MWCNT, the nanocomposite, FSM(SUM-10), and FAM(SUM-10/AC). (e) CV comparison of p-SnTe and p-MWCNT. (f)–(j) CV curves of SUM-3 to SUM-15 at various scan rates exhibiting pseudocapacitive behaviour. (k) and (l) CV profiles of FSM and FAM devices showing ideal capacitive response. (m)–(o) GCD curves of FSM and FAM devices at different current densities, highlighting voltage retention and discharge performance.

and EDLC mechanisms enabled by the synergistic hybrid. The areal capacitance values calculated from CV curves at a scan rate of 5 mV s^{-1} are 416.2, 935.7, 1109.1, and 956.5 mF cm^{-2} for the SUM-3, SUM-5, SUM-10, and SUM-15 nanocomposites, respectively. Among these, the SUM-10 electrode demonstrates the highest areal capacitance (1109.1 mF cm^{-2}, which can be attributed to the optimized incorporation of MWCNTs that provide a conductive framework, facilitate rapid electron transport, and prevent excessive aggregation of SnTe nanoparticles. Notably, the performance decreases slightly at higher loading (SUM-15), suggesting that excess active material induces agglomeration and reduces effective electrochemical surface area. Furthermore, the fabricated symmetric and asymmetric microsupercapacitor (MSC) devices exhibit areal capacitances of 91.5 and 468.6 mF cm^{-2} at 5 mV s^{-1}, respectively, highlighting the superior charge storage capability of the asymmetric configuration. The higher capacitance in the asymmetric device arises from the synergistic contribution of the faradaic and non-faradaic processes, enabling a broader potential window and improved energy storage efficiency compared to the symmetric configuration. These results confirm the potential of SUM-based nanocomposites as promising electrode materials for high-performance flexible microsupercapacitors.

5.3. Galvanostatic charge–discharge (GCD) analysis

To evaluate the rate performance and energy storage capabilities, GCD measurements were carried out, as shown in Fig. 6(m)–(o). The GCD curves of FSM(SUM-10) at different current densities (0.1, 0.5, and 1 mA cm^{-2}) in Fig. 6(m) exhibit linear and nearly symmetric charge/discharge characteristics with minimal IR drop, maintaining a working voltage of up to 0.8 V. The areal capacitance (C_g) was estimated using eqn (4).

$$C_g = \frac{I\Delta t}{S\Delta V} \quad (4)$$

where "ΔV" is the voltage window. In contrast, the FAM(SUM-10//AC) configuration, as shown in Fig. 6(n), sustains a higher operating voltage of 1 V, with extended discharge times at all current densities, emphasizing the improved energy storage due to the hierarchical porous structure of AC. The areal capacitance (C_g) of FAM (SUM-10) is calculated to be 290.2 and 157.6 mF cm^{-2} at current densities of 0.1 and 1 mA cm^{-2}, respectively. Furthermore, eqn (7) was employed to analyse the coulombic efficiency (η), as depicted in Fig. 6(k). In the case of the FAM(SUM-10), the calculated coulombic efficiency (η) is 98.7%. This high efficiency indicates that the device retains a substantial amount of charge throughout its operation, demonstrating its effectiveness in maintaining energy storage performance over time. The efficiency highlights the device's outstanding charge–discharge stability and minimal energy losses, essential for reliable and durable energy storage applications.

$$E_A = \frac{C_s \times (\Delta V)^2}{7200} \quad (5)$$

$$P_A = \frac{3600 \times E_A}{\Delta t} \quad (6)$$

$$\eta = \frac{tD}{tC} \times 100\% \quad (7)$$

Finally, the comparative GCD in Fig. 6(o) shows that FAM(SUM-10//AC) retains superior discharge profiles compared to FSM(SUM-10) under the same current load (0.1 mA cm^{-2}), confirming its enhanced rate capability and long-term electrochemical stability. These results collectively validate the performance superiority of FAM(SUM-10//AC), which benefits from the synergistic integration of conductive networks, porous carbon architecture, and mechanically robust screen-printed design. The energy density (E_A) and power density (E_A) were determined using the standard eqn (5) and (6), respectively. The fabricated device delivered an impressive energy density of 29.05 mW h cm^{-2}, along with a corresponding power density of 418.32 μW cm^{-2}, which surpasses many previously reported results for similar electrode materials as mentioned in Table S1, highlighting the superior charge storage capability and rapid energy delivery of the SUM-based device. The combination of high energy density with considerable power density demonstrates its potential for integration in next-generation flexible and miniaturized energy storage systems.

Furthermore, to demonstrate the practical applicability of the fabricated microsupercapacitor devices, three FAM(SUM-10//AC)-based units were connected in parallel and series configurations, respectively, as shown in Fig. 7(a)–(f). The parallel connection was employed to enhance the overall current handling capability while maintaining the same operational voltage window. In contrast, the series configuration aimed to increase the output voltage, which is essential for powering small-scale electronics. This behaviour confirms the capability of the printed MSCs to operate in real-world applications. The devices also showed robust cycle stability and mechanical flexibility, maintaining their performance under repeated bending and deformation. Such characteristics highlight the potential of FAM(SUM-10//AC)-based microsupercapacitors as integrated, miniaturized energy storage units for next-generation wearable and portable electronic systems. In Fig. 7(a), the Nyquist plot reveals that the parallel configuration exhibits significantly lower charge transfer resistance (R_{ct}) compared to the series configuration, indicating superior ion transport and lower internal resistance.[69] Fig. 7(b) and (d) display cyclic voltammetry (CV) curves of the devices at various scan rates ranging from 5 to 100 mV s^{-1}. The FAM in parallel configuration shows nearly rectangular CV profiles (Fig. 7b), reflecting ideal capacitive behaviour, while the series configuration (Fig. 7d) demonstrates broadened CV areas due to extended voltage windows (up to 3.0 V), which is beneficial for enhanced energy storage.[60] The galvanostatic charge–discharge (GCD) curves shown in Fig. 7(c) and (e) further support these observations, where the FAM in series configuration exhibits prolonged discharge times, indicating higher energy storage capacity. Fig. 7(f) compares the CV curves of symmetric (FSM),

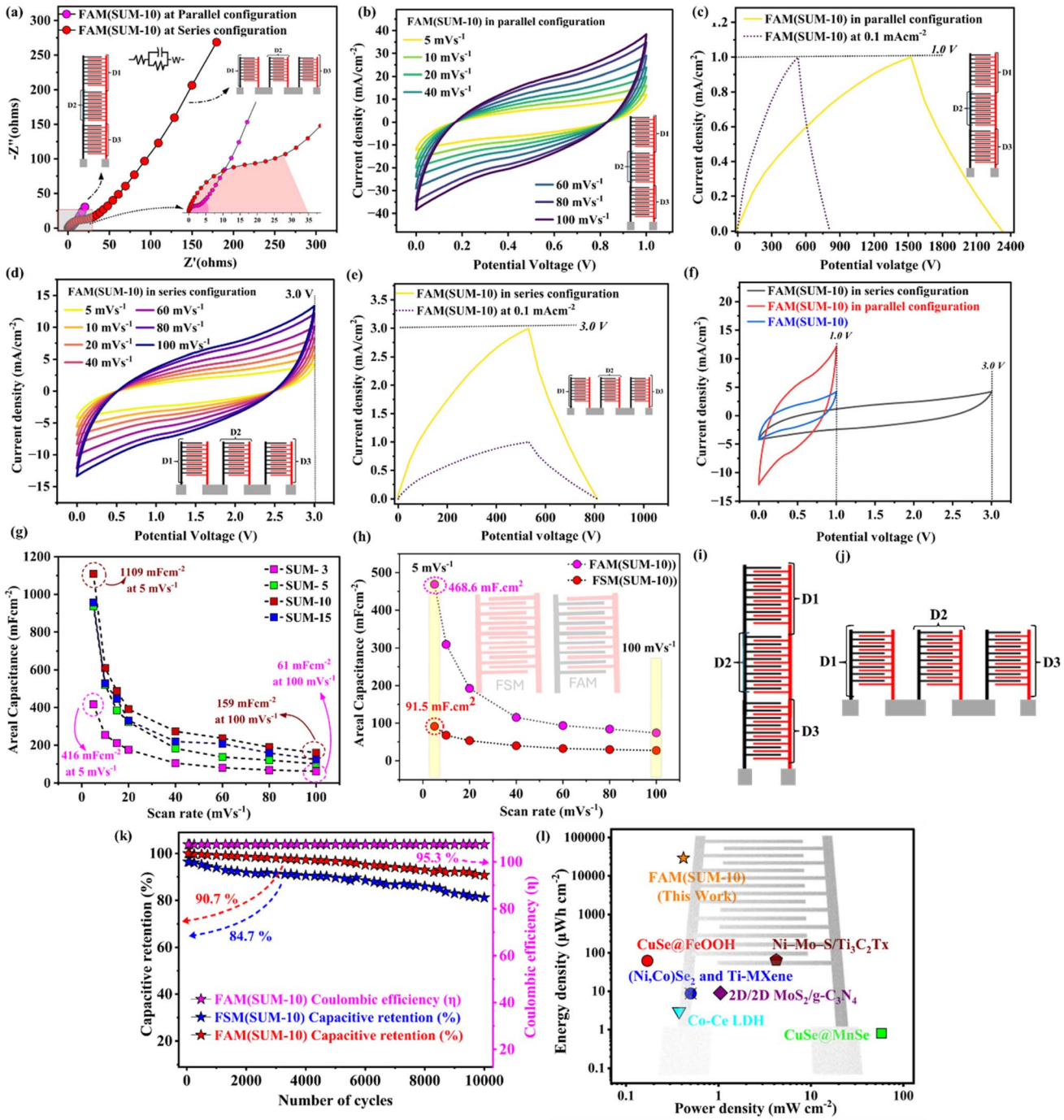

Fig. 7 (a)–(l) Electrochemical evaluation of FAM(SUM-10) in parallel and series configurations: (a) Nyquist plots reveal lower internal resistance in the parallel configuration compared to the series, (b and d) CV curves at varying scan rates (5–100 mV s^{-1}) for parallel and series setups show stable capacitive behaviour, with an extended voltage window up to 3.0 V in series, (c and e) GCD curves at 0.1 mA cm^{-2} confirm near-linear and symmetric charge/discharge profiles, (f) CV comparison of single, parallel, and series devices at 5 mV s^{-1} highlighting voltage scalability, (g) areal capacitance of electrode, (h) FAM configuration outperforms FSM with a maximum capacitance of 468.6 mF cm^{-2}, (i) and (j) schematics illustrating electrode interconnection in parallel and series modes, (k) cycling performance confirms excellent stability with >95.3% retention and high coulombic efficiency over 10 000 cycles, and (l) comparative Ragone for various previously reported microsupercapacitor.

parallel, and series-configured FAM devices at 100 mV s^{-1}, clearly showing that the series configuration offers the highest voltage window and energy output. Areal capacitance comparisons in Fig. 7(g) and (h) highlight that the SUM-10-based FAM device achieves a remarkable areal capacitance of 468.6 mF cm^{-2} at 5 mV s^{-1}, outperforming other compositions (SUM-3, SUM-5, and SUM-15) and the FSM device, which only reached 91.5 mF cm^{-2}. Fig. 7(i) and (j) illustrate the structural configurations of the interdigitated electrodes used in the study, showing clear differentiation between the device architectures.

Finally, Fig. 7(k) demonstrates excellent long-term cycling stability, where the FAM(SUM-10) device retains over 90.7% of its initial capacitance after 10 000 cycles, along with a high coulombic efficiency of approximately 95.3%. Fig. 7(l) shows the comparative analysis of energy and power densities of the present fabricated device with those of previously reported microsupercapacitors, highlighting its comparative electrochemical analysis. Overall, the results confirm the outstanding electrochemical performance, rate capability, and durability of the FAM(SUM-10),[25,28] especially in the series configuration, making it a promising candidate for flexible energy storage applications.

5.4. Flexibility and electrochemical stability under mechanical bending

Fig. S3(a)–(f) illustrate the sequential bending of the FAM(SUM-10) device at various angles (180°, 70°, 30°, 10°, 40°, and back to 180°), demonstrating its mechanical flexibility and durability under repetitive deformation. The electrochemical stability of the device under bending conditions was assessed through cyclic voltammetry (CV) at scan rates of 40 mV s^{-1} and 100 mV s^{-1}, as shown in Fig. S3(g). Prior to bending, the CV curves at both scan rates exhibited a near-rectangular shape, indicative of hybrid behaviour of pseudocapacitive (SnTe/MWCNT) and double layer (AC) behaviour and efficient charge storage. After bending, a slight decrease in current response was observed at both scan rates, which can be attributed to minor strain-induced effects such as microstructural deformation or partial delamination at the electrode/substrate interface. Nevertheless, the CV curves retained their overall shape and symmetry, suggesting that the device maintained excellent electrochemical performance and mechanical integrity even after bending stress. This confirms the robust flexibility of the printed FAM(SUM-10) microsupercapacitor and its suitability for application in deformable and wearable energy storage devices.

5.5. Influence of electrode material deposition on device performance

To evaluate the effect of electrode thickness on device performance, the number of overprints (Ops) was varied during the screen-printing process on PET substrates (Fig. S4(a)–(e)).[70] Fig. S4(a)–(d) depict the effect of the overprinting of the electrode material with increasing Ops. Fig. S4(a) shows the current collector with 3 Ops (10 ± 2 μm thickness), and Fig. S4(b)–(d) show the interdigitated electrode patterns printed with 5, 7, and 9 Ops, resulting in electrode thicknesses of 39.2 μm, 49.2 μm, and 60.4 μm, respectively.[71] Each additional overprint (~5.6 ± 2 μm) increases electrode thickness and active material loading. Five Ops were identified as optimal, significantly enhancing areal capacitance through the synergistic contribution of pseudocapacitive and double-layer charge storage, facilitated by SnTe nanoparticles within the MWCNT framework and the *in situ* grown structure. Beyond this, excessive overprinting (*e.g.*, 9 Ops) causes pattern distortion such as merging and smudging, which can be mitigated by increasing electrode spacing.[72] Fig. S4(e) shows the CV curves of FAM(SUM-10) microsupercapacitors at 0–1 V and 60 mV s^{-1}, confirming enhanced hybrid capacitive behaviour with increasing Ops, peaking at 5–7 Ops. The corresponding areal capacitances are 93.4, 49.5, and 38.08 mF cm^{-2} for 5, 7, and 9 Ops, respectively, calculated using eqn (3). Notably, at 5 Ops, the electrode exhibits optimal performance, with an areal capacitance of 93.4 mF cm^{-2}. A further increase to 7 Ops results in a reduced areal capacitance of 49.5 mF cm^{-2}, while 9 Ops shows a further drop to 38.08 mF cm^{-2}. The decline beyond 5 Ops is mainly due to pattern distortion and smudging, which compromise the electrode resolution and effective surface area, thereby limiting electrochemical performance. The resultant analysis determines that 5 Ops represent the optimal printing condition for balancing film thickness, uniformity, and structural fidelity.

6. Charge storage mechanism for the electrode materials

Fig. 8(a) shows the schematic representation of the charge storage mechanism in the asymmetric supercapacitor based on the SnTe/MWCNTs nanocomposite electrode and activated carbon counter electrode in KOH electrolyte. The working electrode comprises a SnTe/MWCNT nanocomposite printed over a silver current collector, where the synergistic effect of SnTe and MWCNTs enhances electrical conductivity and provides abundant electroactive sites for redox reactions. The counter electrode, composed of activated carbon, contributes primarily through double-layer capacitance. During charging and discharging, K^+ and OH^- ions from the KOH electrolyte migrate between electrodes, where K^+ ions are adsorbed/desorbed at the activated carbon surface, and OH^- ions actively participate in faradaic redox reactions at the SnTe/MWCNT nanocomposite interface.[73,74] The charge storage mechanism of the SnTe/MWCNT electrode was systematically investigated through cyclic voltammetry (CV) at various scan rates to distinguish between capacitive and diffusion-controlled contributions. The relationship between the peak current (i) and scan rate (v) was analysed using Dunn's power law[56,75] (eqn (8)):

$$i = av^b \quad (8)$$

where "i" represents the peak current, "v" is the scan rate, and "a" and "b" are adjustable parameters. The value of b provides insight into the nature of the charge storage mechanism, where "$b = 0.5$" corresponds to a diffusion-controlled process, while "$b = 1.0$" indicates surface-capacitive behaviour. For the SnTe/MWCNT electrode, the b value was calculated to be "0.81", suggesting that the electrochemical response is governed primarily by surface-controlled pseudocapacitive behavior with additional contributions from diffusion-controlled charge storage (Fig. 8(b)). The anodic and cathodic peak currents were further examined, yielding excellent linear fits with correlation coefficients (R^2) of "0.96" and "0.97", respectively (Fig. 8(c)). This high degree of correlation confirms the accuracy and reliability of the Dunn analysis in describing the charge storage kinetics of the SnTe/MWCNT electrode. To quantitatively

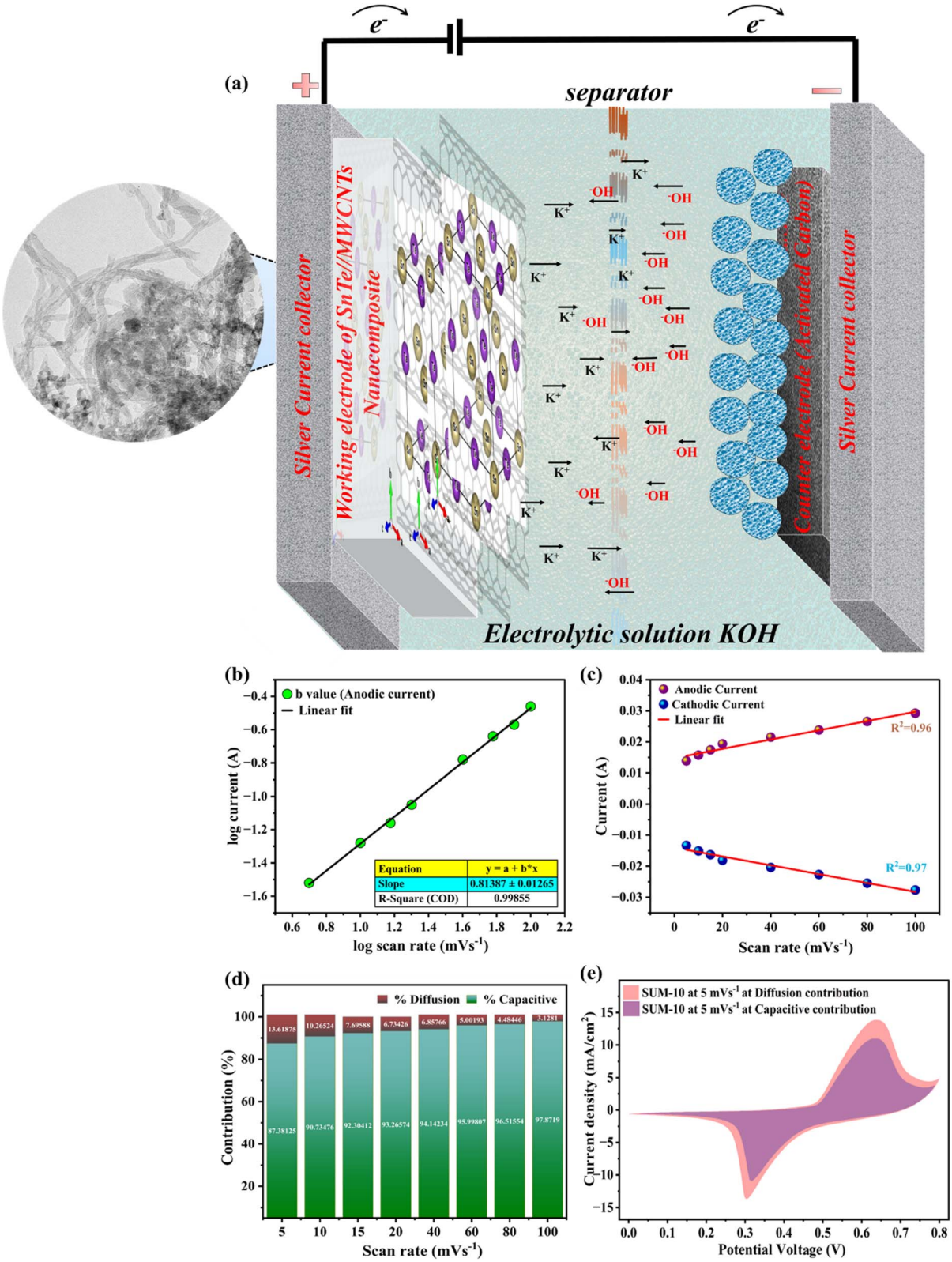

Fig. 8 Electrochemical analysis of the SnTe/MWCNT electrode to elucidate the charge storage mechanism: (a) schematic illustration of ion transport and charge storage behaviour in KOH electrolyte, (b) determination of the *b*-value from the log(*i*) *vs.* log(*v*) relationship, (c) anodic and cathodic peak current dependence on the scan rate with linear fits, (d) quantitative contributions of capacitive- and diffusion-controlled processes at different scan rates, and (e) separation of current response into capacitive and diffusion-controlled components at 5 mV s^{-1}.

differentiate between the two processes, the total current response was deconvoluted according to eqn (9) and (10):

$$\text{surface capacitive processes contribution} = \frac{k_1 V}{k_1 V + k_2 V^{\frac{1}{2}}} \times 100 \quad (9)$$

$$\text{diffusion-controlled contribution} = \frac{k_2 V}{k_1 V + k_2 V^{\frac{1}{2}}} \times 100 \quad (10)$$

The results, shown in Fig. 8(d)–(e), indicate that the capacitive contribution dominates across the entire scan rate range (5–100 mV s^{-1}), while the diffusion-controlled contribution varied between 87.6% and 97.8%. This demonstrates that the SnTe/MWCNT nanocomposite exhibits predominantly capacitive charge storage behaviour, which is favourable for achieving fast charge–discharge kinetics and high-rate capability. The underlying electrochemical mechanism can be attributed to the synergistic effect between SnTe and MWCNTs. The MWCNT network provides rapid electron transport pathways and a large electroactive surface area, while SnTe undergoes reversible faradaic redox reactions with OH^-/K^+ ions from the KOH electrolyte. During the charging process, SnTe participates in surface-controlled redox reactions, while MWCNTs facilitate the formation of an electrical double layer. Conversely, during discharge, electrons are released through the oxidation of SnTe, and ions are desorbed from the MWCNT surface, completing the electrochemical cycle. Overall, the mixed charge storage mechanism, dominated by pseudocapacitive processes, endows the SnTe/MWCNT electrode with superior electrochemical performance. This makes it highly promising for next generation microsupercapacitors requiring both high power density and excellent cycling stability. Furthermore, the comparison of the electrochemical properties of different MSC electrode materials is mentioned in Table S3. The optimized active site density in SUM-10 provides a balanced concentration of electroactive sites, ensuring efficient redox activity without excessive agglomeration, which typically hampers electron and ion transport in higher loadings. The compositional ratio in SUM-10 also facilitates strong interfacial coupling, as observed in high-resolution HRTEM micrographs, between the transition selenide domains and the conductive MWCNT network. This synergistic interaction significantly reduces charge transfer resistance (R_{ct}) and enhances ion diffusion, thereby improving both charge storage and transport. Furthermore, SUM-10 avoids the structural collapse or resistance buildup observed in higher compositions (*e.g.*, SUM-15), preserving long-term electrochemical stability, as evidenced by a capacitance retention of 96.8%, and maintaining the integrity of the conductive pathways, reflected in a high coulombic efficiency of 98.7%. Moreover, the enhanced electrochemical performance of the SnTe/MWCNT nanocomposites originates from interfacial band alignment and charge redistribution at the heterojunction. As shown in Scheme 3, the energy band diagram indicates that MWCNTs possess a relatively higher work function of $\phi = 5.9$ eV compared to SnTe $\phi = 4.5$–5.5 eV.[76,77] When these two p-type materials come into contact, electron transfer from SnTe (lower work function) to MWCNTs (higher work function) occurs until Fermi level equilibration is achieved. This charge transfer results in downward band bending in SnTe near the interface, where the upward band adjustment in MWCNTs leads to an internal built-in potential at the heterointerface. Although both materials are p-type (p–p heterojunction), the work function difference drives interfacial charge redistribution, creating a hole-rich accumulation region in SnTe near the junction.[78–80] The resulting built-in electric field promotes directional charge transport across the interface and reduces the carrier scattering. The interfacial coupling provides multiple advantages over the reduced charge transfer, accelerated electron transport through conductive MWCNT pathways, and improved interfacial conductivity due to the Fermi level alignment, which leads to ion–electron coupling at the electrode/electrolyte interface. Additionally, the narrow band gap of SnTe (0.18 eV), combined with the high conductivity and quasi-metallic nature of MWCNTs, facilitates rapid redox kinetics. The MWCNT network acts as an efficient electron highway, while SnTe contributes pseudocapacitive redox sites. The band bending at the interface lowers the interfacial energy barrier, enabling faster charge transfer during charge/discharge cycling. Therefore, the SnTe/MWCNT heterointerface is not merely a physical mixture but forms an electronically coupled system, where interface band alignment significantly enhances carrier mobility, suppresses recombination losses, and improves the electrochemical kinetics. This synergistic interaction explains the improved electrochemical performance.

7. Humidity sensor characterization

Flexible microhumidity sensors based on SnTe unwrapped multi-walled carbon nanotube (SUM) nanocomposites have shown great promise due to their fast and sensitive response to changes in ambient humidity.[33,81] The presence of oxygen-rich functional groups in functionalized (–COOH) MWCNTs,[82] along with the high aspect ratio and conductive network of SnTe nanoparticles and the conductive tubular structure of MWCNTs, facilitates efficient adsorption and desorption of water molecules. These hydrophilic characteristics enhance surface interaction with moisture, making the composite highly suitable for humidity sensing. To evaluate the sensor's performance, the devices were exposed to controlled relative humidity (RH) environments ranging from 11% to 97% RH at a constant temperature of 25 °C. The humidity levels were regulated using saturated aqueous solutions of specific salts inside a sealed chamber, as detailed in Scheme S4 and Table S4. The sensor's resistance was recorded using a calibrated digital multimeter (Fluke-179), and the sensitivity was calculated using eqn (11). To investigate the humidity sensing performance, a flexible miniaturized humidity sensor was fabricated using a screen-printing technique on a polyethylene terephthalate (PET) substrate as shown in Scheme S4. The sensor featured an overprinted interdigitated electrode structure with a defined single sensing layer. To evaluate the sensor's response to different humidity concentrations, a series of saturated salt solutions were used to

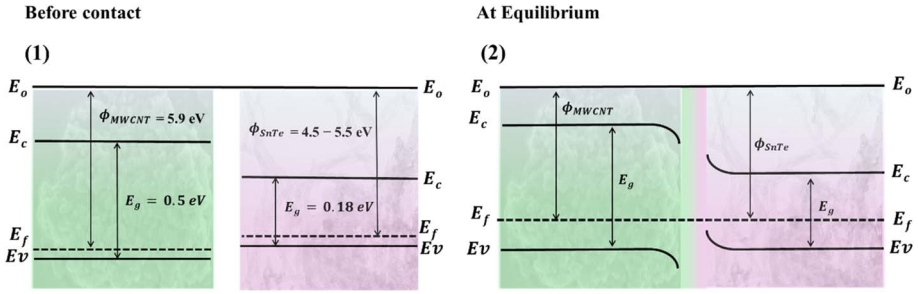

Scheme 3 Energy band diagrams of (1) MWCNTs and SnTe before contact and (2) band alignment of the SnTe/MWCNT heterojunction after Fermi level equilibration. The work function difference induces interfacial charge transfer and band bending.

create controlled relative humidity (%RH) environments ranging from 11% to 97% inside sealed Teflon chambers. These saturated solutions included salts such as LiCl, $MgCl_2$, $Mg(NO_3)_2$, NaCl, KCl, KNO_3, and others, each providing a stable (%RH) level at room temperature. Additionally, the results were also cross-checked using a commercially available humidity probe sensor (Electronic Spices®). The sensor was suspended above the solution (approx. 1.5–2 cm) inside each chamber to ensure exposure to water vapor without direct contact with the liquid phase. The sensor's electrical response was monitored using a precision source meter (multimeter (Fluke®)) connected to a data acquisition system, allowing real-time measurement of resistance variations. The active sensing area (approximately 3.8 mm × 4.3 mm) and electrode spacing (0.5 mm) were optimized for high sensitivity and reproducibility. This setup enabled systematic characterization of the sensor's performance across a wide humidity range.

$$S_R = \frac{R_i - R_{RH}}{R_i} \times 100 \quad (11)$$

where "R_i" denotes the initial resistance at 11% RH, while "R_{RH}" represents the resistance at a specific %RH level. The minimum and maximum responses were calculated using eqn (11) across the "11% to 97% RH" range.

As shown in Fig. 9(a) and (b), a consistent increase in resistance was observed with rising RH levels, indicating a typical p-type semiconducting response driven by water molecule adsorption. This resistance modulation is attributed to the physisorption and subsequent chemisorption of water, leading to the formation of H_3O^+ ions through proton hopping, which alters charge transport pathways in the sensing layer.[82] The enhanced sensitivity in single-layer sensors can be attributed to their thinner active films, which offer minimal diffusion barriers and faster response kinetics. In contrast, triple-printed sensors with thicker films exhibit reduced sensitivity, primarily due to restricted vapour diffusion and delayed interaction with the embedded sensing sites. These findings emphasize the crucial influence of film thickness and nanoscale material synergy in optimizing the humidity sensing performance of SnTe-MWCNT nanocomposites. The humidity sensing performance of the pristine materials, SnTe and MWCNTs, was first evaluated over the RH range of 11% to 97%. SnTe showed a decrease in resistance from 10.87 kΩ to 3.67 kΩ, resulting in a change (ΔR) of 7.20 kΩ. In contrast, MWCNTs exhibited a larger absolute change, from 31.45 kΩ to 20.65 kΩ, corresponding to a ΔR of 10.80 kΩ. Although MWCNTs showed a higher ΔR, SnTe demonstrated a greater relative change in resistance, as evident in Fig. 9(a). To further enhance sensing performance, nanocomposites (SUM-3 to SUM-15) incorporating different proportions of the pristine materials were fabricated and tested. The SUM-3 sensor displayed a resistance drop from 20.67 kΩ to 5.39 kΩ (ΔR = 15.28 kΩ). For SUM-5, the resistance changed from 40.89 kΩ to 27.61 kΩ (ΔR = 13.28 kΩ), while SUM-10 exhibited the highest response, with resistance decreasing from 56.38 kΩ to 3.93 kΩ (ΔR = 52.45 kΩ). In contrast, SUM-15 showed a relatively modest change from 64.67 kΩ to 57.63 kΩ (ΔR = 7.04 kΩ) as shown in Fig. 9(b). These results confirm that SUM-10 offers the most significant resistance variation, indicating optimal synergy between SnTe and MWCNTs, and thus superior sensitivity among the tested nanocomposites. This superior response is attributed to the optimized composition of SUM-10, where the balance between the semiconducting properties of SnTe and the high surface area and conductivity of MWCNTs provides an ideal network for moisture adsorption and charge transport. The synergy between the two components enhances the interaction with water molecules, facilitating efficient electron transfer and significant resistance modulation. Furthermore, the hysteresis, "H" represents the maximum hysteresis, "S" denotes sensitivity, and "ΔH_{max}" is the maximum absolute difference in resistance during adsorption and desorption, measured at 97% RH, as elucidated in eqn (12).

$$H = \frac{\Delta H_{max}}{S} \quad (12)$$

The hysteresis behaviour of the humidity sensor was systematically evaluated by cycling the RH from 11% to 97% (adsorption) and subsequently from 97% to 11% (desorption). The hysteresis curve illustrates the discrepancy between the resistance responses during adsorption and desorption at identical RH levels, indicating the degree of variation in sensor response to RH changes. This phenomenon is primarily attributed to the delayed desorption of water molecules from the active sensing sites, resulting in a looped curve. The extent of hysteresis, quantified as the maximum absolute difference in

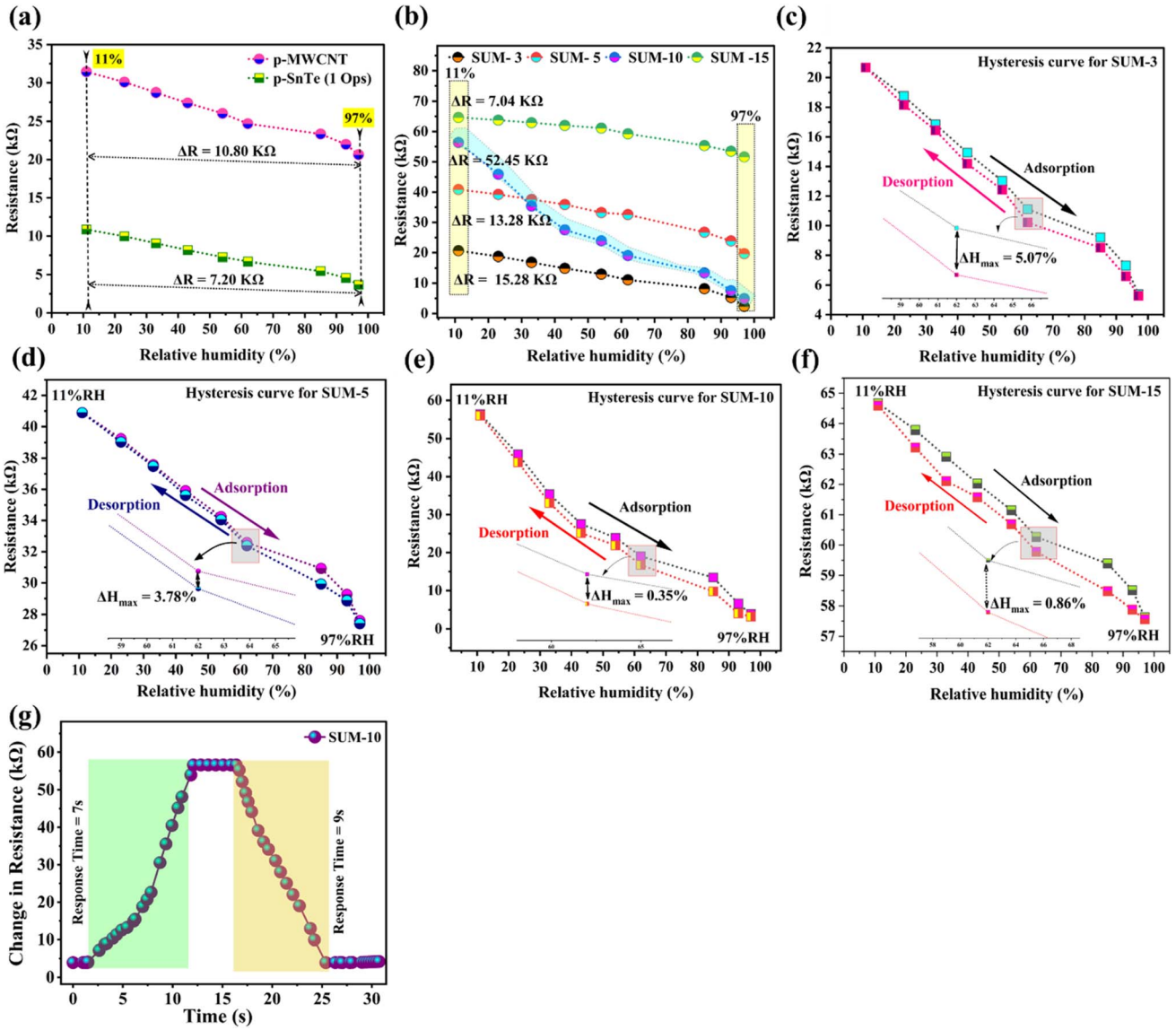

Fig. 9 (a) Resistance variation of pristine p-MWCNT and p-SnTe with increasing RH (11–97%); (b) comparative humidity sensing response of nanocomposites (SUM-3 to SUM-15), highlighting the highest ΔR in SUM-10. Hysteresis curves of resistance response *versus* relative humidity for (c) SUM-3, (d) SUM-5, (e) SUM-10, and (f) SUM-15, showing adsorption and desorption behaviour with corresponding ΔH_{max} values. (g) Dynamic response–recovery behaviour of SUM-10 at varying relative humidity, indicating a response time of 7 s and a recovery time of 9 s.

resistance values at a given RH (typically at 97%), reflects the sensor's reversibility and reliability for repeated use in dynamic humidity conditions. Fig. 9(c)–(f) show the hysteresis curve for the prepared nanocomposites (SUMs). The hysteresis behaviour of fabricated sensors SUM-3(c), SUM-5(d), SUM-10(e), and SUM-15(f) was analysed to evaluate their reversibility and stability. The hysteresis values were determined by calculating the maximum resistance difference ΔH_{max} between adsorption and desorption at a fixed RH level and normalizing it by the sensitivity (S) across the RH range of 11–97%. Among these, SUM-10 exhibited the lowest hysteresis of 0.35%, followed by SUM-15 at 0.86%, while SUM-5 and SUM-3 recorded significantly higher hysteresis values of 3.78% and 5.07%, respectively. The superior hysteresis performance of SUM-10 and SUM-15 highlights their excellent reversibility, minimal signal drift, and efficient desorption kinetics, which are essential for reliable long-term sensing applications. These sensors likely benefit from optimized surface morphology, homogeneous nanocomposite dispersion, and controlled porosity, which facilitate rapid and reversible interactions with water molecules. In contrast, the larger hysteresis observed in SUM-3 and SUM-5 suggests incomplete desorption and possible moisture trapping within the sensing layer, likely due to less favourable surface energetics or aggregation effects. The low hysteresis exhibited by SUM-10 at 62% RH confirms their potential as promising candidates for high-performance, stable, and reusable humidity sensors suitable for integration into flexible and wearable electronic systems. Furthermore, the SUM-10 based nanocomposite

exhibits a distinct response and recovery behaviour at a specific relative humidity of 85% RH. Over the course of time-resolved analysis, the material demonstrates a rapid and stable change in resistance, clearly highlighting its sensitivity to moisture adsorption during the response (7 s) phase and efficient desorption during the recovery (9 s) phase, as shown in Fig. 9(g). This consistent performance under controlled humidity conditions confirms the reliability and reproducibility of SUM-10 as a potential candidate for high-performance humidity sensing applications.

7.1. Humidity sensing mechanism

The humidity sensing mechanism is primarily governed by the interaction between water vapour molecules and the surface of the sensing material, as shown in Scheme 4. When the sensor is exposed to varying levels of relative humidity (%RH), the adsorption of water molecules causes measurable changes in its electrical properties, particularly resistance or capacitance.[83] At low humidity levels, water molecules initially undergo physisorption, forming a monolayer on the sensor surface through weak van der Waals forces. This thin layer does not significantly contribute to proton conduction, and hence, the resistance remains relatively high. As humidity increases, multilayer adsorption takes place, and water molecules start forming a continuous network.[84] This allows for the Grotthuss chain reaction mechanism,[82] where protons (H^+) hop between adjacent water molecules. This enhances ionic conductivity and decreases the resistance of the material. In nanocomposite systems such as SnTe/MWCNT, the mechanism is further enhanced due to the high surface area and porous structure provided by the carbon nanotubes. These features allow for better water molecule trapping and faster diffusion paths. The semiconducting nature of SnTe facilitates charge transport, and the composite structure ensures a synergistic effect, improving both the sensitivity and response time of the sensor. Moreover, the presence of defect sites, oxygen-containing functional groups, and interfaces between different phases (such as SnTe and MWCNT) contributes to polar interactions with water molecules, further aiding adsorption and enhancing sensor performance. The sensor exhibits a decrease in resistance with rising humidity, which is reversible upon desorption, enabling real-time humidity monitoring.[85,86] The synergistic behaviour of SnTe and MWCNTs in the humidity sensing application is primarily governed by the Te–Sn bonds, which act as hydrophilic adsorption centres for H_2O molecules. The proton hopping mechanism, as discussed earlier, facilitates rapid conductivity modulation, which is essential for high-performance sensing. In the optimized nanocomposite, the synergy between Sn and Te ensures high sensitivity through strong interactions with water molecules, while the MWCNTs provide a stable conductive network, maintaining a wide dynamic range and minimizing hysteresis during adsorption/desorption cycles. This unified mechanism, where SnTe nodes function as the active sensing sites and MWCNTs serve as conductive highways, establishes a cooperative framework in which ion–electron coupling underlies both charge storage (electrochemical) and signal modulation (humidity sensing).

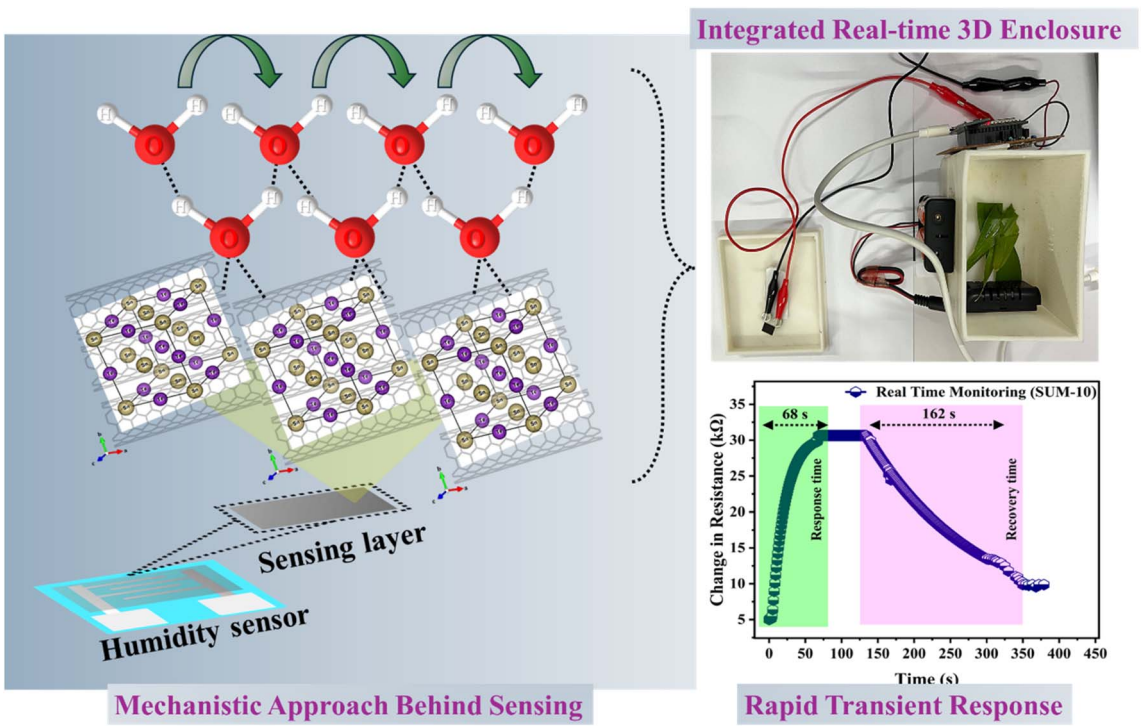

Scheme 4 Schematic representation of the sensing mechanism in the fabricated humidity sensor, where water molecules interact with the sensing layer, leading to changes in resistance. The integrated real-time 3D enclosure setup for device testing is shown along with the transient response curve.

8. Real-time monitoring using the fabricated environmental monitoring assembly

For real-time monitoring, prototypes were fabricated to demonstrate the integration of a humidity sensing device with a microcontroller-based system for environmental applications. The device housing was fabricated using fused deposition modeling (FDM) 3D printing with a polylactic acid (PLA) filament,[87] and the complete design and printing details are provided in SI Scheme S5(a)–(c). As shown in Fig. 10(a), the setup features a commercial humidity sensor positioned within a custom 3D-printed chamber housing fresh green leaves, thereby simulating a natural humidity source generated by crops. The commercial sensor was connected to a microcontroller for real-time monitoring, with the measured humidity displayed on a small screen. In parallel, the fabricated SnTe/MWCNT-based humidity sensor, optimized for high sensitivity, was mounted on the chamber lid at a fixed distance of 4 cm above the leaves. This sensor was connected to an ESP32 microcontroller and interfaced with Arduino® software, enabling continuous resistance measurements as a function of time. The fabricated sensor exhibited a fast response time of 68 s and a recovery time of 162 s, attributed to the high conductivity of MWCNTs, which promotes rapid adsorption and desorption of water molecules. In Fig. 10(b), the compact assembly of the microcontroller and associated circuitry is shown, affixed to the side of the enclosure for portability and easy deployment. The sensor–microcontroller unit was connected through a breadboard-based interface for signal processing. Fig. 10(c) presents the wireless data acquisition setup, where real-time sensor output was transmitted to a laptop and visualized using a custom dashboard. Fig. 10(d) shows the microcontroller assembly and supporting electronic components, while Fig. 10(e) displays the dynamic resistance response curve of the fabricated device using the SUM-10 sensor, confirming stable and reproducible performance during repeated humidification cycles. Comparative summary of previously reported sensing materials for flexible humidity sensors, arranged according to response time. The table highlights the influence of the material structure, synthesis method, and sensing principle on device performance, as shown in Table S5. Overall, the prototype demonstrates a low-cost, non-invasive, and portable real-time humidity sensing system, highlighting its potential for environmental monitoring and agricultural applications.

8.1. Device integration and applications

The fabricated flexible interdigitated microsupercapacitors (MSCs) and humidity sensors demonstrate significant potential for next-generation wearable and portable electronics. Both devices benefit from screen-printing fabrication, a scalable and cost-effective technique that supports large-area, high-throughput production while maintaining device performance. The use of flexible substrates (*e.g.*, PET) enables integration into bendable and lightweight platforms, essential for wearable and IoT-based systems.[88,89]

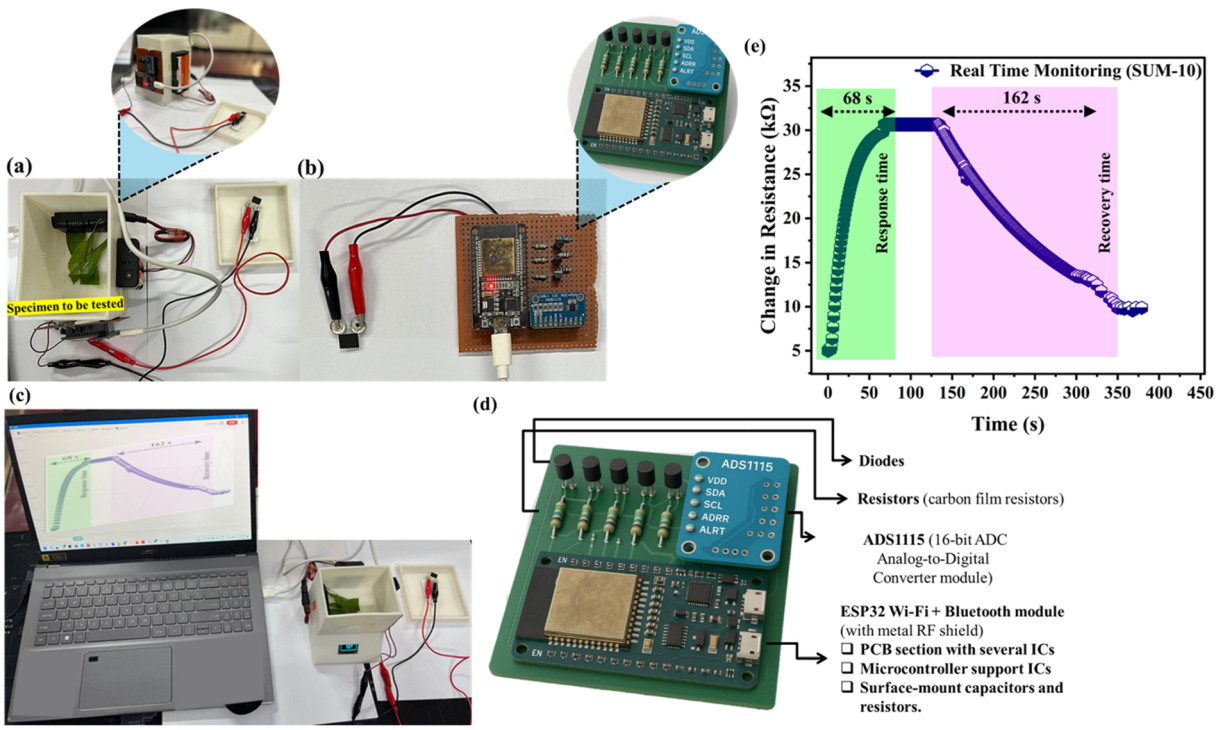

Fig. 10 (a)–(d) Real-time humidity sensing setup with microcontroller integration, (a) sensor enclosed in a 3D-printed chamber with natural leaf samples, (b) portable sensor microcontroller assembly, (c) wireless data acquisition and visualization on a laptop, (d) microcontroller assembly with supporting components, and (e) response curve showing dynamic resistance change during humidity exposure and recovery.

For MSCs, the high areal capacitance, rapid charge/discharge capability, and long-term cycling stability allow efficient powering of low-energy IoT nodes, sensors, and microelectronics, reducing reliance on bulky or non-sustainable batteries. Their ability to be configured in series or parallel further enhances design flexibility to meet specific voltage and energy requirements. For humidity sensors, the rapid response/recovery behaviour and high sensitivity make them ideal for real-time environmental monitoring. They are inherently IoT-compatible, with potential applications in healthcare (*e.g.*, respiratory tracking and wound healing assessment), agriculture, and industrial process monitoring.[33,90] Their flexible and miniaturized design enables seamless embedding into textiles, packaging, and wearable devices. From a market standpoint, both MSCs and humidity sensors are aligned with the growing demand for sustainable, eco-friendly technologies. The use of green conductive inks and binder systems not only supports environmental goals but also strengthens their relevance for consumer electronics and smart sensing markets. Collectively, these devices offer scalable, IoT-ready, and market-relevant solutions for future intelligent and connected systems.

9. Conclusion

A polycrystalline SnTe/MWCNT (SUM) nanocomposite was synthesized *via* a Bridgman-type method and used to fabricate flexible microsupercapacitors and humidity sensors by screen printing. The SUM nanocomposite synergistically combines SnTe's high pseudocapacitance with the conductivity, flexibility, and porous architecture of MWCNTs, overcoming the limitations of pristine SnTe. The asymmetric SUM-10 device delivered a high areal capacitance of 468.6 mF cm^{-2} at 5 mV s^{-1}, excellent rate capability with a capacitance retention of 90.7% (FAM) and 84.7% (FSM), and superior cycling stability with a coulombic efficiency of 95.3% over 10 000 cycles under repeated bending. As a humidity sensor, SUM-10 exhibited rapid response (68 s) and recovery (162 s) times, high sensitivity, and reliable performance during deformation. Furthermore, a real-time monitoring prototype was demonstrated using FDM 3D printing integrated with a microcontroller for continuous humidity tracking. These results establish SUM-10 as a promising dual-functional platform that combines high-performance energy storage with real-time environmental monitoring, opening pathways for its application in wearable electronics, IoT, and precision agriculture.

Conflicts of interest

The authors declare the following competing interests: Mohammad Saquib, Shilpa Shetty, Ramakrishna Nayak and M. Selvakumar have filed a patent entitled "Polycrystalline growth methods for MWCNT–SnTe nanocomposites and applications in flexible printed electronics" (Patent Application No. 202541126417) with Manipal Academy of Higher Education (MAHE). The other authors declare no competing interests.

Data availability

The data supporting this article are included in the supplementary information (SI). Supplementary information: detailed experimental procedures, screen-printing methodology, characterization techniques, electrochemical performance data, humidity sensing evaluation, additional figures and schemes (S1–S5), and tables (S1–S5). Further data supporting the findings of this study are available from the corresponding author upon reasonable request. See DOI: https://doi.org/10.1039/d5ta10103d.

Acknowledgements

Mohammad Saquib is grateful for the Dr T. M. A. Pai Fellowship from the Manipal Academy of Higher Education for his doctoral research.

References

1 K. Dissanayake and D. Kularatna-Abeywardana, A review of supercapacitors: Materials, technology, challenges, and renewable energy applications, *J. Energy Storage*, 2024, **96**, 112563, DOI: 10.1016/j.est.2024.112563.
2 A. K. Kamali, E. Glogic, N. M. Keppetipola, G. Sonnemann, T. Toupance and L. Cojocaru, Prospective Life Cycle Assessment of Two Supercapacitor Architectures, *ACS Sustain. Chem. Eng.*, 2023, **11**, 15898–15909, DOI: 10.1021/acssuschemeng.3c04007.
3 S. Poonam, K. Sharma, A. Arora and S. K. Tripathi, Review of supercapacitors: Materials and devices, *J. Energy Storage*, 2019, **21**, 801–825, DOI: 10.1016/j.est.2019.01.010.
4 S. Karthikeyan, B. Narenthiran, A. Sivanantham, L. D. Bhatlu and T. Maridurai, Supercapacitor: Evolution and review, *Mater. Today: Proc.*, 2021, **46**, 3984–3988, DOI: 10.1016/j.matpr.2021.02.526.
5 D. Corzo, G. Tostado-Blázquez and D. Baran, Flexible Electronics: Status, Challenges and Opportunities, *Front. Electron.*, 2020, **1**, 594003, DOI: 10.3389/felec.2020.594003.
6 M. Saquib, R. Nayak, D. Devadiga, M. Selvakumar, S. Paramasivam, C. Ghosh, Y. N. Sudhakar and S. Senthilkumar, Printed flexible supercapacitor from conductive ink of graphite nanocomposite blended with Co3O4 to facilitate the fabrication of energy storage device, *J. Energy Storage*, 2023, **72**, 108800, DOI: 10.1016/j.est.2023.108800.
7 Z. Liu, F. Mo, H. Li, M. Zhu, Z. Wang, G. Liang and C. Zhi, Advances in Flexible and Wearable Energy-Storage Textiles, *Small Methods*, 2018, **2**, 1800124, DOI: 10.1002/smtd.201800124.
8 V. L. Pushparaj, M. M. Shaijumon, A. Kumar, S. Murugesan, L. Ci, R. Vajtai, R. J. Linhardt, O. Nalamasu and P. M. Ajayan, Flexible energy storage devices based on nanocomposite paper, *Proc. Natl. Acad. Sci. U. S. A.*, 2007, **104**, 13574–13577, DOI: 10.1073/pnas.0706508104.
9 S. A. Delbari, L. S. Ghadimi, R. Hadi, S. Farhoudian, M. Nedaei, A. Babapoor, A. Sabahi Namini, Q. Van Le,

M. Shokouhimehr, M. Shahedi Asl and M. Mohammadi, Transition metal oxide-based electrode materials for flexible supercapacitors: A review, *J. Alloys Compd.*, 2021, **857**, 158281, DOI: 10.1016/j.jallcom.2020.158281.

10 Y.-Z. Z. Zhang, T. Cheng, Y. Wang, W.-Y. Y. Lai, H. Pang and W. Huang, A Simple Approach to Boost Capacitance: Flexible Supercapacitors Based on Manganese Oxides@MOFs *via* Chemically Induced *In Situ* Self-Transformation, *Adv. Mater.*, 2016, **28**, 5242–5248, DOI: 10.1002/adma.201600319.

11 M. Saquib, S. Shetty, L. M, A. Rathod, K. Naik, R. Nayak and M. Selvakumar, Challenges in carbon ink formulation and strategies for fabrication of flexible supercapacitors, *Carbon Trends*, 2025, **19**, 100458, DOI: 10.1016/j.cartre.2025.100458.

12 Y. Kabalci, E. Kabalci, S. Padmanaban, J. B. Holm-Nielsen and F. Blaabjerg, Internet of Things Applications as Energy Internet in Smart Grids and Smart Environments, *Electronics*, 2019, **8**, 972, DOI: 10.3390/electronics8090972.

13 S. Mehta, S. Jha and H. Liang, Lignocellulose materials for supercapacitor and battery electrodes: A review, *Renewable Sustainable Energy Rev.*, 2020, **134**, 110345, DOI: 10.1016/j.rser.2020.110345.

14 W. Raza, F. Ali, N. Raza, Y. Luo, K.-H. Kim, J. Yang, S. Kumar, A. Mehmood and E. E. Kwon, Recent advancements in supercapacitor technology, *Nano Energy*, 2018, **52**, 441–473, DOI: 10.1016/j.nanoen.2018.08.013.

15 D. B. Olawade, O. Z. Wada, A. O. Ige, B. I. Egbewole, A. Olojo and B. I. Oladapo, Artificial intelligence in environmental monitoring: Advancements, challenges, and future directions, *Hyg. Environ. Health Adv.*, 2024, **12**, 100114, DOI: 10.1016/j.heha.2024.100114.

16 L. Gong, Z. Wang, J. Zhao, J. Tang, Z. Li, W. Meng, Z. Qiu, Y. Qin, X. Wang, C. Zhang and D. Zhang, High-performance supercapacitor and ultra-sensitive humidity sensor based on bifunctional NiCo2O4/g-C3N4 nanocomposites powered by triboelectric nanogenerator, *Chem. Eng. J.*, 2023, **477**, 147087, DOI: 10.1016/j.cej.2023.147087.

17 C. Paeng, A. Shanmugasundaram, G. We, T. Kim, J. Park, D.-W. Lee and C. Yim, Rapid and Flexible Humidity Sensor Based on Laser-Induced Graphene for Monitoring Human Respiration, *ACS Appl. Nano Mater.*, 2024, **7**, 4772–4783, DOI: 10.1021/acsanm.3c05283.

18 Y. Lu, K. Jiang, D. Chen and G. Shen, Wearable sweat monitoring system with integrated micro-supercapacitors, *Nano Energy*, 2019, **58**, 624–632, DOI: 10.1016/j.nanoen.2019.01.084.

19 J. R. McGhee, J. S. Sagu, D. J. Southee, P. S. A. Evans and K. G. U. Wijayantha, Printed, Fully Metal Oxide, Capacitive Humidity Sensors Using Conductive Indium Tin Oxide Inks, *ACS Appl. Electron. Mater.*, 2020, **2**, 3593–3600, DOI: 10.1021/acsaelm.0c00660.

20 G. Guarnieri, B. Olivieri, G. Senna and A. Vianello, Relative Humidity and Its Impact on the Immune System and Infections, *Int. J. Mol. Sci.*, 2023, **24**, 9456, DOI: 10.3390/ijms24119456.

21 S. A. Khan, M. M. Rehman, S. Iqbal, M. M. Baig, S. G. Lee and W. Y. Kim, Wireless flexi-sensor using narrow band quasi colloidal 3D tin telluride (SnTe) for respiratory, environment, and proximity sensing, *Chem. Eng. J.*, 2024, **495**, 153376, DOI: 10.1016/j.cej.2024.153376.

22 M. Hultberg, C. Oskarsson, K.-J. Bergstrand and H. Asp, Benefits and drawbacks of combined plant and mushroom production in substrate based on biogas digestate and peat, *Environ. Technol. Innovation*, 2022, **28**, 102740, DOI: 10.1016/j.eti.2022.102740.

23 A.-R. Park and C.-M. Park, Cubic Crystal-Structured SnTe for Superior Li- and Na-Ion Battery Anodes, *ACS Nano*, 2017, **11**, 6074–6084, DOI: 10.1021/acsnano.7b02039.

24 M. Z. Ansari, S. A. Ansari and S.-H. Kim, Fundamentals and recent progress of Sn-based electrode materials for supercapacitors: A comprehensive review, *J. Energy Storage*, 2022, **53**, 105187, DOI: 10.1016/j.est.2022.105187.

25 C. D. Jadhav, G. P. Patil, S. Lyssenko and R. Minnes, Hot-injected ligand-free SnTe nanoparticles: a cost-effective route to flexible symmetric supercapacitors, *J. Mater. Chem. A*, 2025, **13**, 2822–2835, DOI: 10.1039/d4ta07111e.

26 S. Zhang, D. Yang, M. Zhang, Y. Liu, T. Xu, J. Yang and Z.-Z. Yu, Synthesis of novel bimetallic nickel cobalt telluride nanotubes on nickel foam for high-performance hybrid supercapacitors, *Inorg. Chem. Front.*, 2020, **7**, 477–486, DOI: 10.1039/c9qi01395d.

27 X. Wei, X. Wang, X. Tan, Q. An and L. Mai, Nanostructured Conversion-Type Negative Electrode Materials for Low-Cost and High-Performance Sodium-Ion Batteries, *Adv. Funct. Mater.*, 2018, **28**, 1804458, DOI: 10.1002/adfm.201804458.

28 M. Abdullah, P. John, K. F. Fawy, S. Manzoor, K. Y. Butt, A. G. Abid, M. Messali, M. Najam-Ul-Haq and M. N. Ashiq, Facile synthesis of the SnTe/SnSe binary nanocomposite *via* a hydrothermal route for flexible solid-state supercapacitors, *RSC Adv.*, 2023, **13**, 12009–12022, DOI: 10.1039/d3ra01028g.

29 B. Nan, X. Song, C. Chang, K. Xiao, Y. Zhang, L. Yang, S. Horta, J. Li, K. H. Lim, M. Ibáñez and A. Cabot, Bottom-Up Synthesis of SnTe-Based Thermoelectric Composites, *ACS Appl. Mater. Interfaces*, 2023, **15**, 23380–23389, DOI: 10.1021/acsami.3c00625.

30 G. Han, R. Zhang, S. Popuri, H. Greer, M. Reece, J.-W. Bos, W. Zhou, A. Knox and D. Gregory, Large-Scale Surfactant-Free Synthesis of p-Type SnTe Nanoparticles for Thermoelectric Applications, *Materials*, 2017, **10**, 233, DOI: 10.3390/ma10030233.

31 M. Yang, W. Zhang, D. Su, J. Wen, L. Liu and X. Wang, Flexible SnTe/carbon nanofiber membrane as a free-standing anode for high-performance lithium-ion and sodium-ion batteries, *J. Colloid Interface Sci.*, 2022, **605**, 231–240, DOI: 10.1016/j.jcis.2021.07.110.

32 T. Delipinar, A. Shafique, M. S. Gohar and M. K. Yapici, Fabrication and Materials Integration of Flexible Humidity Sensors for Emerging Applications, *ACS Omega*, 2021, **6**, 8744–8753, DOI: 10.1021/acsomega.0c06106.

33 B. Arman Kuzubasoglu, Recent Studies on the Humidity Sensor: A Mini Review, *ACS Appl. Electron. Mater.*, 2022, **4**, 4797–4807, DOI: 10.1021/acsaelm.2c00721.

34 M. R. Shankar, A. N. Prabhu, A. Rao, U. D. Shanubhogue and B. Srinivasan, Potential improvement in thermoelectric properties of SnTe polycrystals *via* anionic and cationic substitution, *Ceram. Int.*, 2024, **50**, 46869–46881, DOI: 10.1016/j.ceramint.2024.09.037.

35 Z. Yuan, G. Chen, D. Zhou, P. Liu, L. Liu, S. Fan and K. Jiang, Carbon Nanostructure-Enabled High-Performance Thermal Insulation for Extreme-Temperature Application, *Adv. Funct. Mater.*, 2026, **36**(9), e14142, DOI: 10.1002/adfm.202514142.

36 G. A. Rance, D. H. Marsh, S. J. Bourne, T. J. Reade and A. N. Khlobystov, van der Waals Interactions between Nanotubes and Nanoparticles for Controlled Assembly of Composite Nanostructures, *ACS Nano*, 2010, **4**, 4920–4928, DOI: 10.1021/nn101287u.

37 F. C.-M. Leung, S. Y.-L. Leung, C. Y.-S. Chung and V. W.-W. Yam, Metal–Metal and π–π Interactions Directed End-to-End Assembly of Gold Nanorods, *J. Am. Chem. Soc.*, 2016, **138**, 2989–2992, DOI: 10.1021/jacs.6b01382.

38 E. M. Pérez and N. Martín, π–π interactions in carbon nanostructures, *Chem. Soc. Rev.*, 2015, **44**, 6425–6433, DOI: 10.1039/c5cs00578g.

39 Y. Liu, B. Zhang, Q. Xu, Y. Hou, S. Seyedin, S. Qin, G. G. Wallace, S. Beirne, J. M. Razal and J. Chen, Development of Graphene Oxide/Polyaniline Inks for High Performance Flexible Microsupercapacitors *via* Extrusion Printing, *Adv. Funct. Mater.*, 2018, **28**, 1706592, DOI: 10.1002/adfm.201706592.

40 B. Balan, S. Ramasamy, S. P. Rajendra, M. S. AlSalhi and S. Angaiah, Advanced (Cu,Co)Se 2 Nanocubes and Ti-MXene Based Screen Printed Electrodes for High Performance Flexible Microsupercapacitors, *Adv. Funct. Mater.*, 2024, **34**(48), 2408639, DOI: 10.1002/adfm.202408639.

41 P. Giannakou, M. G. Masteghin, R. C. T. Slade, S. J. Hinder and M. Shkunov, Energy storage on demand: ultra-high-rate and high-energy-density inkjet-printed NiO micro-supercapacitors, *J. Mater. Chem. A*, 2019, **7**, 21496–21506, DOI: 10.1039/c9ta07878a.

42 Y. Lin, J. Chen, M. M. Tavakoli, Y. Gao, Y. Zhu, D. Zhang, M. Kam, Z. He and Z. Fan, Printable Fabrication of a Fully Integrated and Self-Powered Sensor System on Plastic Substrates, *Adv. Mater.*, 2019, **31**(5), 1804285, DOI: 10.1002/adma.201804285.

43 D. Li, W. Lai, Y. Zhang and W. Huang, Printable Transparent Conductive Films for Flexible Electronics, *Adv. Mater.*, 2018, **30**(10), 1704738, DOI: 10.1002/adma.201704738.

44 A. Nag, A. Mitra and S. C. Mukhopadhyay, Graphene and its sensor-based applications: A review, *Sens. Actuators, A*, 2018, **270**, 177–194, DOI: 10.1016/j.sna.2017.12.028.

45 Y. Liao, R. Zhang, H. Wang, S. Ye, Y. Zhou, T. Ma, J. Zhu, L. D. Pfefferle and J. Qian, Highly conductive carbon-based aqueous inks toward electroluminescent devices, printed capacitive sensors and flexible wearable electronics, *RSC Adv.*, 2019, **9**, 15184–15189, DOI: 10.1039/c9ra01721f.

46 A. Prakash, S. R. Holla, S. Selvaraj, R. Nayak, S. De, M. Saquib and M. Selvakumar, Highly conducting Laser-Induced Graphene-Ag nanoparticle composite as an effective supercapacitor electrode with anti-fungal properties, *Sci. Rep.*, 2024, **14**, 27849, DOI: 10.1038/s41598-024-79382-3.

47 J. O. Kim, J. Y. Kim, J. C. Lee, S. Park, H. R. Moon and D. P. Kim, Versatile Processing of Metal-Organic Framework-Fluoropolymer Composite Inks with Chemical Resistance and Sensor Applications, *ACS Appl. Mater. Interfaces*, 2019, **11**, 4385–4392, DOI: 10.1021/acsami.8b19630.

48 J. Ning, K. Men, G. Xiao, B. Zou, L. Wang, Q. Dai, B. Liu and G. Zou, Synthesis of narrow band gap SnTe nanocrystals: nanoparticles and single crystal nanowires *via* oriented attachment, *CrystEngComm*, 2010, **12**, 4275, DOI: 10.1039/c004098n.

49 N. T. K. Thanh, N. Maclean and S. Mahiddine, Mechanisms of Nucleation and Growth of Nanoparticles in Solution, *Chem. Rev.*, 2014, **114**, 7610–7630, DOI: 10.1021/cr400544s.

50 X. Teng, J. Chen, B. Sun, M. Liu, C. Qi, H. Song, F. Xiong and J. He, Study on the nucleation and growth of In2O3 powders for oxide ceramic targets, *J. Alloys Compd.*, 2022, **921**, 166130, DOI: 10.1016/j.jallcom.2022.166130.

51 A. Güngör, Enhanced supercapacitor performance with cerium-doped polypyrrole nanofibers, *J. Mater. Chem. A*, 2025, **13**, 18641–18655, DOI: 10.1039/d5ta02164b.

52 N. Berchenko, R. Vitchev, M. Trzyna, R. Wojnarowska-Nowak, A. Szczerbakow, A. Badyla, J. Cebulski and T. Story, Surface oxidation of SnTe topological crystalline insulator, *Appl. Surf. Sci.*, 2018, **452**, 134–140, DOI: 10.1016/j.apsusc.2018.04.246.

53 W. Yao, C. Tian, C. Yang, J. Xu, Y. Meng, I. Manke, N. Chen, Z. Wu, L. Zhan, Y. Wang and R. Chen, P-Doped NiTe 2 with Te-Vacancies in Lithium–Sulfur Batteries Prevents Shuttling and Promotes Polysulfide Conversion, *Adv. Mater.*, 2022, **34**, DOI: 10.1002/adma.202106370.

54 X. Li, S. Sun, N. Wang, B. Huang and X. Li, SnTe/SnSe Heterojunction Based Ammonia Sensors with Excellent Withstand to Ambient Humidities, *Small*, 2024, **20**(23), 2309831, DOI: 10.1002/smll.202309831.

55 M. W. Hakim, I. Ali, S. Fatima, H. Li, S. H. M. Jafri and S. Rizwan, Enhanced Electrochemical Performance of MWCNT-Assisted Molybdenum–Titanium Carbide MXene as a Potential Electrode Material for Energy Storage Application, *ACS Omega*, 2024, **9**, 8763–8772, DOI: 10.1021/acsomega.3c04932.

56 S. M. Ali, H. Kassim and M. S. Amer, Nanoarchitectonics of tin telluride: A novel pseudocapacitive material for energy storage application, *Mater. Chem. Phys.*, 2023, **301**, 127698, DOI: 10.1016/j.matchemphys.2023.127698.

57 J. Iqbal, A. Numan, S. Rafique, R. Jafer, S. Mohamad, K. Ramesh and S. Ramesh, High performance supercapattery incorporating ternary nanocomposite of multiwalled carbon nanotubes decorated with Co3O4 nanograins and silver nanoparticles as electrode material,

Electrochim. Acta, 2018, **278**, 72–82, DOI: 10.1016/j.electacta.2018.05.040.

58 O. V. Kharissova and B. I. Kharisov, Variations of interlayer spacing in carbon nanotubes, *RSC Adv.*, 2014, **4**, 30807–30815, DOI: 10.1039/c4ra04201h.

59 R. Nayak, P. Shetty, S. M, A. Rao, S. K V, S. Wagle, S. Nayak, V. Kamath, N. Shetty and M. Saquib, Formulation and optimization of copper selenide/PANI hybrid screen printing ink for enhancing the power factor of flexible thermoelectric generator: A synergetic approach, *Ceram. Int.*, 2024, **50**, 25779–25791, DOI: 10.1016/j.ceramint.2024.04.315.

60 M. Saquib, R. Nayak, M. Selvakumar, D. K. Bhat and C. S. Rout, Enhanced flexibility and performance of interdigitated microsupercapacitors through *in situ* rGO growth in NiCuSe nanocomposite conductive ink, *J. Alloys Compd.*, 2025, **1027**, 180574, DOI: 10.1016/j.jallcom.2025.180574.

61 Y. Gao, J. Feng, F. Liu and Z. Liu, Effects of Organic Vehicle on the Rheological and Screen-Printing Characteristics of Silver Paste for LTCC Thick Film Electrodes, *Materials*, 2022, **15**, 1953, DOI: 10.3390/ma15051953.

62 H. Hong, H. Jiyong, K.-S. Moon, X. Yan and C. Wong, Rheological properties and screen printability of UV curable conductive ink for flexible and washable E-textiles, *J. Mater. Sci. Technol.*, 2021, **67**, 145–155, DOI: 10.1016/j.jmst.2020.06.033.

63 C. O' Mahony, E. U. Haq, C. Silien and S. A. M. Tofail, Rheological Issues in Carbon-Based Inks for Additive Manufacturing, *Micromachines*, 2019, **10**, 99, DOI: 10.3390/mi10020099.

64 G. Greco, A. Giuri, S. Bagheri, M. Seiti, O. Degryse, A. Rizzo, C. Mele, E. Ferraris and C. E. Corcione, Pedot:PSS/Graphene Oxide (GO) Ternary Nanocomposites for Electrochemical Applications, *Molecules*, 2023, **28**, 2963, DOI: 10.3390/molecules28072963.

65 J. Liang, C. Jiang and W. Wu, Printed flexible supercapacitor: Ink formulation, printable electrode materials and applications, *Appl. Phys. Rev.*, 2021, **8**(2), 021319, DOI: 10.1063/5.0048446.

66 K. Shen, J. Ding and S. Yang, 3D Printing Quasi-Solid-State Asymmetric Micro-Supercapacitors with Ultrahigh Areal Energy Density, *Adv. Energy Mater.*, 2018, **8**(20), 1800408, DOI: 10.1002/aenm.201800408.

67 R. Nayak, P. Shetty, S. M, A. Rao and K. M. Rao, Formulation of new screen printable PANI and PANI/Graphite based inks: Printing and characterization of flexible thermoelectric generators, *Energy*, 2022, **238**, 121680, DOI: 10.1016/j.energy.2021.121680.

68 O. S. Toker, S. Karasu, M. T. Yilmaz and S. Karaman, Three interval thixotropy test (3ITT) in food applications: A novel technique to determine structural regeneration of mayonnaise under different shear conditions, *Food Res. Int.*, 2015, **70**, 125–133, DOI: 10.1016/j.foodres.2015.02.002.

69 R. Kumar, M. Singh and A. Soam, Study on electrochemical properties of silicon micro particles as electrode for supercapacitor application, *Surf. Interfaces*, 2020, **19**, 100524, DOI: 10.1016/j.surfin.2020.100524.

70 X. Li, S. Xiong, G. Li, S. Xiao, C. Zhang and Y. Ma, Effect of microstructure on electrochemical performance of electrode materials for microsupercapacitor, *Mater. Lett.*, 2023, **346**, 134481, DOI: 10.1016/j.matlet.2023.134481.

71 B. Nie, X. Li, J. Shao, C. Li, P. Sun, Y. Wang, H. Tian, C. Wang and X. Chen, Scalable fabrication of high-performance micro-supercapacitors by embedding thick interdigital microelectrodes into microcavities, *Nanoscale*, 2019, **11**, 19772–19782, DOI: 10.1039/c9nr05247j.

72 L. Jiang, S. Wang, F. Meng, J. Hu and X. Yan, The influence of electrode geometry on the electrochemical performance of fabric-based screen-printed coplanar supercapacitors, *J. Energy Storage*, 2023, **73**, 109001, DOI: 10.1016/j.est.2023.109001.

73 I. Denmark, S. Macchi, F. Watanabe, T. Viswanathan and N. Siraj, Effect of KOH on the Energy Storage Performance of Molasses-Based Phosphorus and Nitrogen Co-Doped Carbon, *Electrochem*, 2021, **2**, 29–40, DOI: 10.3390/electrochem2010003.

74 A. Patra, N. K, J. R. Jose, S. Sahoo, B. Chakraborty and C. S. Rout, Understanding the charge storage mechanism of supercapacitors: in situ/operando spectroscopic approaches and theoretical investigations, *J. Mater. Chem. A*, 2021, **9**, 25852–25891, DOI: 10.1039/d1ta07401f.

75 Y. Liu, S. P. Jiang and Z. Shao, Intercalation pseudocapacitance in electrochemical energy storage: recent advances in fundamental understanding and materials development, *Mater. Today Adv.*, 2020, **7**, 100072, DOI: 10.1016/j.mtadv.2020.100072.

76 Q. Fu, P. Lyu, S. Handschuh-Wang, L. Teng and B. Zheng, Facile synthesis of hierarchical Co3O4/MWCNT composites with enhanced acetone sensing property, *Ceram. Int.*, 2022, **48**, 28419–28427, DOI: 10.1016/j.ceramint.2022.06.155.

77 X. Wang, J. Liu, R. Li, J. Yu, Q. Liu, J. Zhu and P. Liu, Hierarchical Nanoheterostructure of HFIP-Grafted α-Fe_2O_3@Multiwall Carbon Nanotubes as High-Performance Chemiresistive Sensors for Nerve Agents, *Nanomaterials*, 2024, **14**, 305, DOI: 10.3390/nano14030305.

78 G. Jamwal, A. Kumar, M. Warish, S. Chakravarty, S. Muthiah, A. Kandasami and A. Niazi, Structural, electronic and thermoelectric properties of SnTe with dilute co-doping of Ag and Cu, *J. Alloys Compd.*, 2023, **954**, 170182, DOI: 10.1016/j.jallcom.2023.170182.

79 G. Tan, L.-D. Zhao, F. Shi, J. W. Doak, S.-H. Lo, H. Sun, C. Wolverton, V. P. Dravid, C. Uher and M. G. Kanatzidis, High Thermoelectric Performance of p-Type SnTe *via* a Synergistic Band Engineering and Nanostructuring Approach, *J. Am. Chem. Soc.*, 2014, **136**, 7006–7017, DOI: 10.1021/ja500860m.

80 D. Park, H. Ju, T. Oh and J. Kim, A p-type multi-wall carbon nanotube/Te nanorod composite with enhanced thermoelectric performance, *RSC Adv.*, 2018, **8**, 8739–8746, DOI: 10.1039/c7ra13572f.

81 H. Farahani, R. Wagiran and M. Hamidon, Humidity Sensors Principle, Mechanism, and Fabrication

Technologies: A Comprehensive Review, *Sensors*, 2014, **14**, 7881–7939, DOI: 10.3390/s140507881.

82 Y. S. S. Al-Faiyz and M. Gouda, Multi-Walled Carbon Nanotubes Functionalized with Hydroxamic Acid Derivatives for the Removal of Lead from Wastewater: Kinetics, Isotherm, and Thermodynamic Studies, *Polymers*, 2022, **14**, 3870, DOI: 10.3390/polym14183870.

83 M. Saquib, S. Shiraj, R. Nayak, A. Nirmale and M. Selvakumar, Synthesis and Fabrication of Graphite/WO3 Nanocomposite-Based Screen-Printed Flexible Humidity Sensor, *J. Electron. Mater.*, 2023, **52**, 4226–4238, DOI: 10.1007/s11664-023-10404-y.

84 R. Kumar and B. C. Yadav, Fabrication of Polyaniline (PANI)—Tungsten oxide (WO3) Composite for Humidity Sensing Application, *J. Inorg. Organomet. Polym. Mater.*, 2016, **26**, 1421–1427, DOI: 10.1007/s10904-016-0412-9.

85 N. Sun, Z. Ye, X. Kuang, W. Liu, G. Li, W. Bai and X. Tang, High sensitivity capacitive humidity sensors based on $Zn_{1-x}Ni_xO$ nanostructures and plausible sensing mechanism, *J. Mater. Sci.:Mater. Electron.*, 2019, **30**, 1724–1738, DOI: 10.1007/s10854-018-0445-7.

86 I. Popov, Z. Zhu, A. R. Young-Gonzales, R. L. Sacci, E. Mamontov, C. Gainaru, S. J. Paddison and A. P. Sokolov, Search for a Grotthuss mechanism through the observation of proton transfer, *Commun. Chem.*, 2023, **6**, 77, DOI: 10.1038/s42004-023-00878-6.

87 X. Wang, L. Huang, Y. Li, Y. Wang, X. Lu, Z. Wei, Q. Mo, S. Zhang, Y. Sheng, C. Huang, H. Zhao and Y. Liu, Research progress in polylactic acid processing for 3D printing, *J. Manuf. Process.*, 2024, **112**, 161–178, DOI: 10.1016/j.jmapro.2024.01.038.

88 G. Scandurra, A. Arena and C. Ciofi, A Brief Review on Flexible Electronics for IoT: Solutions for Sustainability and New Perspectives for Designers, *Sensors*, 2023, **23**, 5264, DOI: 10.3390/s23115264.

89 Y. Zhan, Y. Mei and L. Zheng, Materials capability and device performance in flexible electronics for the Internet of Things, *J. Mater. Chem. C*, 2014, **2**, 1220–1232, DOI: 10.1039/c3tc31765j.

90 K. Liao, F. Wang, Q. Shen, Y. Liu, Z. Mei, H. Wang, S. Zhang, S. Ma and L. Wang, Advances in humidity sensors based on Self-Powered technology, *Chem. Eng. J.*, 2025, **505**, 159480, DOI: 10.1016/j.cej.2025.159480.